From Rotation Curves to Cosmic Time: Probing High-Redshift Expansion through Nested Spiral Dynamicss

E.P.J. de Haas[1, a)]

Kandinsky College, Nijmegen, The Netherlands

We present a novel method for estimating the cosmic expansion rate H_z at high redshift ($z \approx 2$–10) using the internal dynamics and morphology of nearby galaxies—without relying on direct redshift–distance measurements. The approach models rotation curves of systems showing a clear structural transition between a central bar (interpreted as a fossil spiral) and an outer spiral disk. Within a dual-Lagrangian framework, these nested structures are assigned separate dynamical regimes, enabling H_z to be extracted from the mass M and *critical radius* r_c of the proto-bar region. The critical radius is defined locally by the condition $v_H(r_c) = v_{\rm esc}(r_c)$, which yields a *local critical density* $\rho_c \propto H_z^2$. When this purely local relation is mapped onto cosmic time using the ΛCDM matter-era scaling $H(t) \propto t^{-1}$, it reproduces the universal $\rho_c \propto t^{-2}$ law. Applying the method to seventeen galaxies, and scanning early bulge mass fractions from 0.2% to 20% of today's $M_{\rm bulge}$, we find that the 0.5%–5% range best matches the ΛCDM timeline for disk–spiral onset. A refined backward-time minimization, incorporating a power-law bulge growth model, further narrows the plausible onset window to 0.4–1.8 Gyr after the Big Bang. This technique complements high-redshift probes such as *JWST* imaging and CMB extrapolations, offering a new class of local, dynamical constraints on the early universe. If validated and applied to large rotation-curve samples, it could yield hundreds to thousands of independent H_z determinations, refining both the cosmic expansion history and the baryonic structure formation timeline.

PACS numbers: 98.62.Dm, 98.80.-k, 98.80.Es, 98.62.Gq, 98.62.Ai

Keywords: Hubble parameter, galaxy rotation curves, early universe, nested spiral structure, cosmic expansion

[a)]Electronic mail: haas2u@gmail.com

I. OVERVIEW OF MODELING FRAMEWORK EVOLUTION

The theoretical framework presented in this paper evolved through a sequence of modeling refinements, each driven by the goal of improving the physical realism and explanatory power of galactic rotation curve fits. This progression not only deepens our understanding of galactic structure but ultimately enables a novel, physically grounded estimation of the local expansion rate H_z in the early universe.

We begin with a single-region model for individual galaxies, assuming a constant Lagrangian metric inflow within a symmetric baryonic bulge. In this regime, spiral inflow velocities can be expressed as a combination of tangential metric motion and radial metric components, encoded via a fixed effective potential. The effective potential incorporates Newtonian gravity and Hubble expansion through a superposition of respective metric velocities. This initial framework offers a good match for certain galaxies where the baryonic structure is dominated by a central bulge, but proves insufficient when confronted with more complex rotation curves.

To address this, the model is extended to incorporate *multi-region virial transitions*. By defining physically distinct domains—such as the bulge interior, a first pure metric spiral disk region, and an outer region with additional virial motion—the rotation curve can be decomposed into segments with different dynamical behaviors. This segmentation leads to more accurate fits and reveals structural transitions not visible in the single-region model.

However, some galaxies exhibit rotation curves that cannot be reproduced by a single galaxy wide Lagrangian, even with multiple regions, but can be fit using two constant Lagrangian curves. We now interpret these systems as displaying clear signatures of *nested spirals*: an inner, bar-like structure (interpreted as a relic spiral) and an outer disk spiral, each with distinct dynamical histories and possibly formed at different cosmic epochs. To capture this, the model is generalized to include two distinct Lagrangians—one for the inner bulge-bar spiral, one for the outer disk spiral—each characterized by its own radius, mass, and expansion parameter H_z. The outer disk spiral appears like a reset of the original bulge by including the mass of the bar and starting at the outer realm of the bulge-bar system, its visible or invisible ring with its specific critical radius.

Finally, by treating the inner bulge-bar as a fossil remnant of an earlier structural phase, i.e., a proto-galaxy, and assuming it constituted a small fraction (e.g., 0.2–5%) of today's bulge mass, we derive an independent estimate of the early-universe expansion rate H_z via the local condition $v_H = v_{\text{esc}}$ at the bar–ring-disk transition radius. This condition depends solely on the measured M and

r_c of an individual galaxy and is therefore independent of cosmological assumptions. Only after mapping H_z to cosmic time using the global ΛCDM $H(t)$ relation—based on chosen cosmological parameters—do the local measurements converge with the large-scale matter-era scaling $\rho \propto t^{-2}$.

This hierarchical modeling—from single-region fits to nested spirals, to the locally anchored $v_H = v_{\rm esc}$ condition, and finally to its cosmological interpretation—forms the backbone of the present analysis and underpins the results discussed in the sections that follow.

II. PROGRESSIVE ADAPTATION OF THE CONSTANT LAGRANGIAN INFLOW MODEL TO REAL GALACTIC DYNAMICS

A. Rotation Curve Fit for UGC 1281 Using the Metric Inflow Model

To assess the capability of the metric inflow model to describe real galactic rotation curves, we applied it to the dwarf galaxy UGC 1281, using the SPARC database [4]. The primary objective was to determine whether the full radial profile of the orbital velocity squared $v^2(r)$ could be accurately reproduced using only parameters with direct physical interpretation—namely the bulge radius R, the enclosed mass M, and the cosmological expansion rate $H(z)$. The orbital velocity squared is modeled by two distinct regimes:

Inside the bulge ($r \leq R$):

$$v_{orb}^2(r) = \frac{1}{2}\left(\sqrt{\frac{2GM}{R}} - H_z R\right)^2 \cdot \frac{r^2}{R^2} \tag{1}$$

Outside the bulge ($r > R$):

$$v_{orb}^2(r) = \frac{3}{2}\left(\sqrt{\frac{2GM}{R}} - H_z R\right)^2 - \left(\sqrt{\frac{2GM}{r}} - H_z r\right)^2 \tag{2}$$

We began by manually estimating the bulge radius $R_{\rm bulge}$ using visual fitting techniques in a dedicated Excel analysis. This step aimed to identify the transition point between the inner solid-body rotation and the outer flattened region. Based on this inspection, we adopted $R_{\rm bulge} = 1.968\,\text{kpc}$ as the best estimate and held it fixed during the automated fitting procedure. The best-fit parameters obtained were: Bulge mass: $M = 1.38 \times 10^{39}\,\text{kg}$; bulge radius $R = 1.968\,\text{kpc}$; Hubble parameter: $H_z = 2.30 \times 10^{-18}\,\text{s}^{-1}$; RMS relative residual: 0.065 (in units of km^2/s^2).

Figure 1 displays the best-fit v^2 curve, which shows excellent agreement with the full rotation curve of UGC 1281. The model accurately reproduces both the rising inner region and the

extended flat portion without invoking a dark matter halo profile.

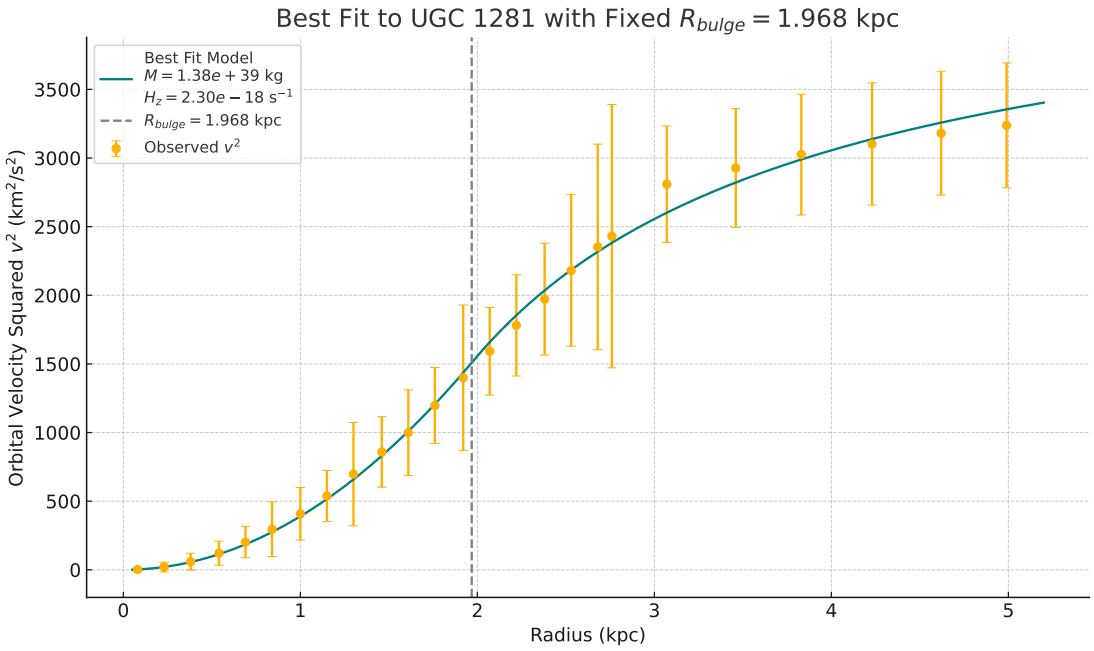

FIG. 1. Best-fit orbital velocity-squared profile $v^2(r)$ for UGC 1281, using the metric inflow model.

Figure 2 presents the residuals between the observed and modeled v^2, plotted with realistic error bars propagated from the velocity uncertainties. On general, the distribution of residuals exhibits no overall systematic deviation and remains within observational noise levels, confirming the quality of the fit.

B. Interpretation of Outer Rotation Curve as Newtonian Orbit in a Moving Metric Frame

By examining the residuals and the behavior of the data in the outer disk, although without overall systematic deviation, we identify the onset of a localized systematic deviation—visible as a highly localizedd consistent overshoot/undershoot in v^2_{data} compared to the model. More specifically, in Figure 2, the last six datapoints develop in a non random way from overshoot to undershoot. So for the randomness of the residuals as a whole, it wouldn't stand out, but as a set of six datapoints it does. That is where we suspected a virial dynamics. By subtracting the inflow-predicted orbital velocity squared v^2_{model} from the SPARC rotation curve data, we isolated the residual component that, in our interpretation, corresponds to standard Newtonian motion.

As shown in Figures 3 and 4, the last six outermost datapoints of UGC 1281 yield residuals

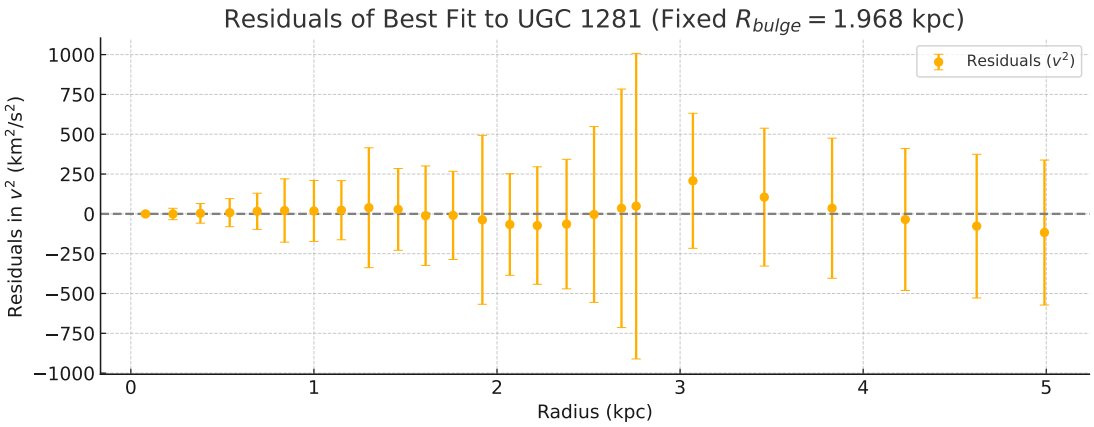

FIG. 2. Residuals in orbital velocity-squared v^2 between the observed rotation curve of UGC 1281 and the best-fit model using the metric inflow formalism. The bulge radius was fixed at $R_{\text{bulge}} = 1.968\,\text{kpc}$, while the mass M and the Hubble parameter H_z were fitted to minimize the weighted residual. Error bars reflect observational uncertainties propagated into v^2. The distribution is consistent with observational noise, supporting the quality of the fit.

that align closely with a Newtonian potential profile $v^2 = GM/r$, after applying a constant vertical shift. This shift accounts for the fact that the residuals are measured in the observer's frame, while the Newtonian orbit occurs within the local comoving metric frame of the orbiting material. The next question was how to incorporate this in the fitting model without tampering with the raw SPARC data.

We decided for continuation of the effective potential and thus introduced a virial term that for the involved masses acted as the only potential present, because relative to the inflowing metric to which they were inertially connected, they didn't experience any other force. The virial term is not applied uniformly but begins to contribute beyond a galaxy-specific radius r_{virial}, located somewhere between the bulge radius R and the critical inflow radius r_c. The value of r_{virial} is determined empirically through analysis of the residuals of the galaxy's rotation curve. In our three-region model, the transition between region 2 (bulge-dominated inflow dynamics) and region 3 (where additional virial orbital corrections are applied) is governed by a parameter r_{virial}. This radius is not directly derived from the analytic model but must be identified empirically. Specifically, we first fit the rotation curve using only regions 1 and 2. Once identified, we introduced a r_{virial} as a fixed input in the subsequent three-region fit. This two-stage approach ensures that the inclusion of the virial correction is not arbitrarily fitted but justified by a clear structural feature in

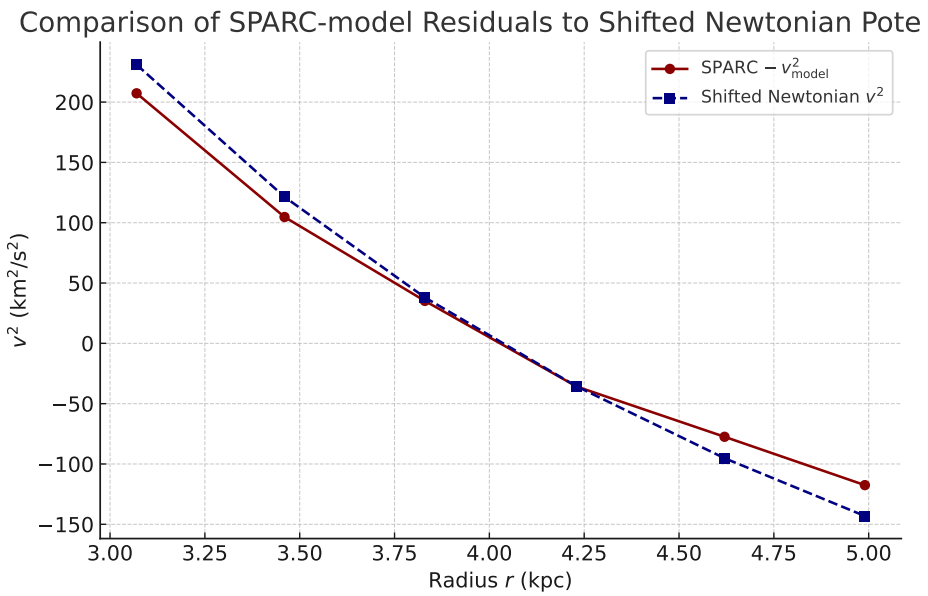

FIG. 3. Comparison of the SPARC–model residuals for the last six outermost data points of UGC 1281 (red circles) with a Newtonian orbital velocity squared profile (blue squares) based on the bulge mass $M = 1.38 \times 10^{39}\,\text{kg}$. The Newtonian curve $v^2 = \frac{GM}{r}$ was shifted vertically by $\Delta v^2 \approx -741.3\,\text{km}^2/\text{s}^2$ to match the residual profile. The agreement suggests that the outer residuals are consistent with a gravitational tail from the bulge alone, without invoking an additional dark matter halo or a modifacation of Newtonian dynamics.

the rotation curve. A parameter Φ_D is a gauge parameter for the virial term, which needs further explanation, but we will not examine that here.

C. Application to UGC 1281

In the case of UGC 1281, residuals from the original two-region metric model displayed a distinct systematic behavior in the outermost six datapoints. The observed v^2 first exceeded the predicted value and then dropped below it—characteristic of a transition to virial orbital motion.

Introducing the full virial term,

$$v^2_{\text{orb}}(r) = \frac{3}{2}\left(\sqrt{\frac{2GM}{R}} - H_z R\right)^2 - \left(\sqrt{\frac{2GM}{r}} - H_z r\right)^2 + \left[\frac{1}{2}\left(\sqrt{\frac{2GM}{r}} - H_z r\right)^2 - \Phi_D\right], \quad (3)$$

for $r \geq r_\Phi$, slightly reduced the RMS of the relative residual from approximately $6,5\%$ to $6,3\%$, demonstrating a small improvement in fit accuracy, see Figure 5 and Figure 6. This fit not only

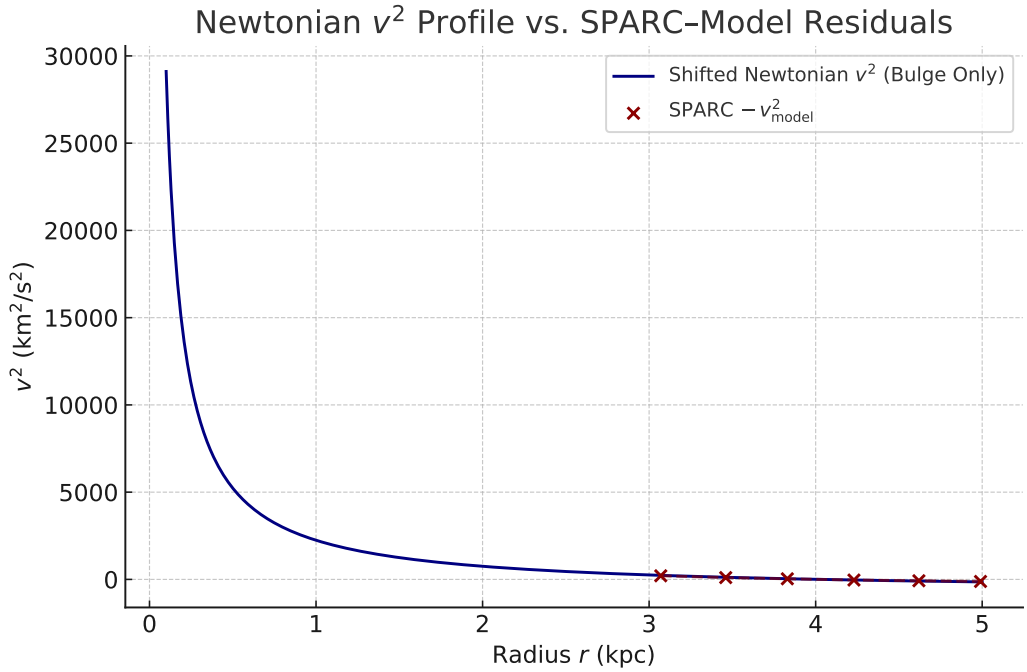

FIG. 4. Comparison between the Newtonian gravitational potential profile of the UGC 1281 bulge and the observed SPARC–model residuals. The blue curve shows the Newtonian orbital velocity squared, computed as $v^2 = \frac{GM}{r}$, for a bulge mass of $M = 1.38 \times 10^{39}\,\text{kg}$ and fixed radius. The curve has been vertically shifted by $\Delta v^2 \approx -741.3\,\text{km}^2/\text{s}^2$ to best align with the SPARC–model residuals from the outer six data points (shown in red). This alignment suggests that the residual structure is consistent with the Newtonian tail of the central bulge, reinforcing the model's interpretation that no additional halo is needed to explain the rotation curve.

reproduced the shape of the rotation curve but also corrected the systematic bias observed in the residuals, affirming the physical relevance of the virial contribution associated with disk dynamics.

D. The virial model applied to NGC 2366: two virial regions

A key success of the metric inflow model is its ability to iteratively improve the fit to galactic rotation curves through the structured inclusion of physically motivated corrections. We demonstrate this through a stepwise refinement of the velocity model applied to NGC 2366 [4], for which we refined the virial term and introduced the possibility to introduce two virial terms for galactic rotation curves. This led to a potential four region approach:

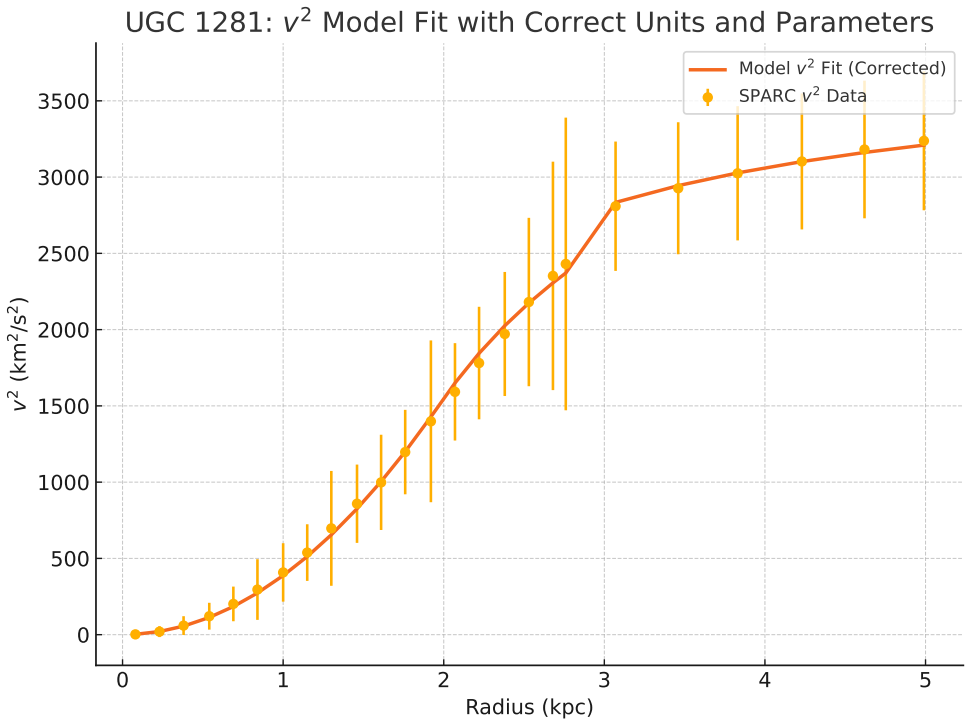

FIG. 5. Rotation curve fit for UGC 1281 using the three-region inflow metric model. The data points represent the observed SPARC rotation curve values v^2 with error bars. The model is constructed using three regions: (1) solid-body rotation inside the bulge, (2) Lagrangian inflow region from the bulge radius up to the virial transition radius, and (3) an outer region including a virial correction term. Model parameters: bulge radius $R = 1.97\,\text{kpc}$, virial transition radius $r_{\text{virial}} = 3.0\,\text{kpc}$, mass $M = 1.376 \times 10^{39}\,\text{kg}$, Hubble parameter $H_z = 2.1841 \times 10^{-18}\,\text{s}^{-1}$, and virial offset $\Phi_D = 716\,\text{km}^2/\text{s}^2$.

Inside the bulge ($r \leq R$)**:**

$$v_{orb}^2(r) = \frac{1}{2}\left(\sqrt{\frac{2GM}{R}} - H_z R\right)^2 \cdot \frac{r^2}{R^2} \tag{4}$$

Outside the bulge until the first virial region ($R < r < r_{virial_1}$):

$$v_{orb}^2(r) = \frac{3}{2}\left(\sqrt{\frac{2GM}{R}} - H_z R\right)^2 - \left(\sqrt{\frac{2GM}{r}} - H_z r\right)^2 \tag{5}$$

Outside the bulge for the first virial region ($r_{virial_1} < r < r_{virial_1}$):

$$v_{orb}^2(r) = \frac{3}{2}\left(\sqrt{\frac{2GM}{R}} - H_z R\right)^2 - \left(\sqrt{\frac{2GM}{r}} - H_z r\right)^2 + \left[p\frac{1}{2}\left(\sqrt{\frac{2GM}{r}} - H_z r\right)^2 - \Phi_p\right] \tag{6}$$

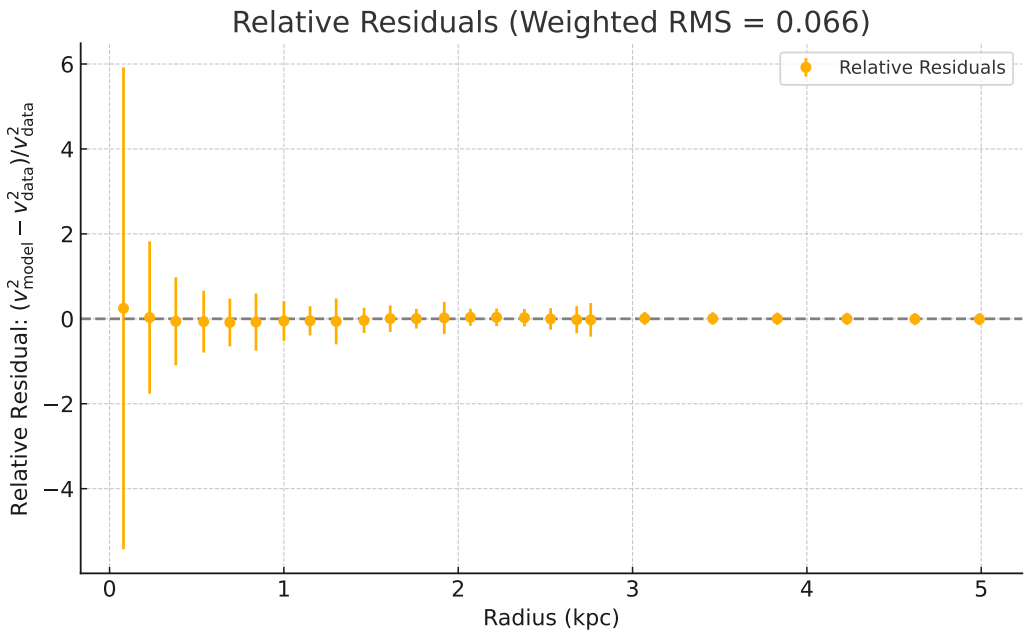

FIG. 6. Relative residuals of the rotation curve fit for UGC 1281 using the three-region Lagrangian inflow model with a virial correction beyond $r_{\text{virial}} = 3\,\text{kpc}$. The bulge radius was fixed at $R = 1.97\,\text{kpc}$, the bulge mass at $M = 1.376 \times 10^{39}\,\text{kg}$, the cosmic expansion rate at $H_z = 2.1841 \times 10^{-18}\,\text{s}^{-1}$, and the virial offset parameter $\Phi_D = 716\,(\text{km/s})^2$. The weighted root mean square (RMS) of the relative residuals is ~ 0.063, demonstrating excellent agreement between the model and the observational SPARC data.

Outside the bulge for the second virial region ($r_{virial_2} < r < rc$):

$$v^2_{orb}(r) = \frac{3}{2}\left(\sqrt{\frac{2GM}{R}} - H_z R\right)^2 - \left(\sqrt{\frac{2GM}{r}} - H_z r\right)^2 + \left[q\frac{1}{2}\left(\sqrt{\frac{2GM}{r}} - H_z r\right)^2 - \Phi_q\right] \tag{7}$$

We toke p and Φ_p and q and Φ_q as a free parametera, reflecting the natural history and orbital independence of the virial mass relative to the Lagrangian inflowing metric. The virial mass can flow with or against the Lagrangian tangential motion of the metric, its orbit can be in an inclined plane relative to the metric inflow of the spiral disk and it might be affected by the additional mass inbetween R and r_{virial}. So introducing two relatively free parameters per virial region seems theoretically and empirically justified. It allowed us to maintain the overal influence of M, R, and Hz over all regions. We define r_{virial} empirically, by visual inspection of the first virial free iteration of the fit of the rotation curve. After identification, the r_{virial} parameters setting the boundaries are fixed.

The result can be seen in Fig.(7), where we have two virial regions, with the first appearing

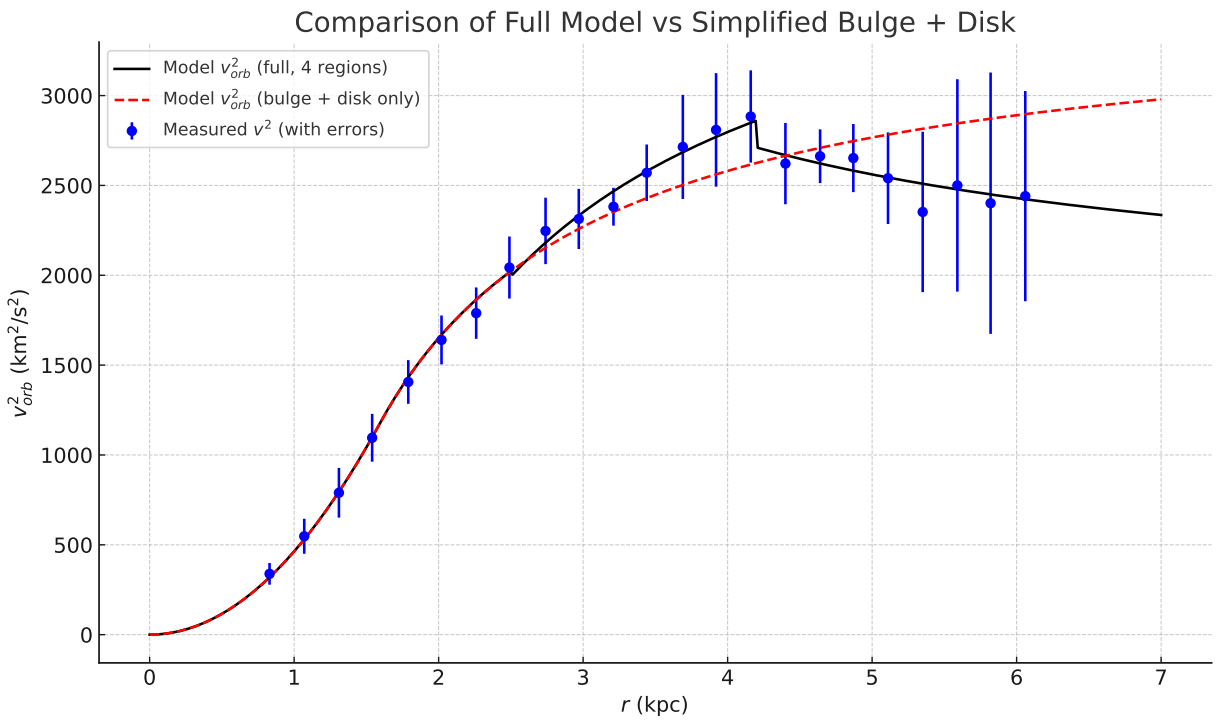

FIG. 7. Comparison between the full 4-region model (solid black) and the simplified bulge + disk model (dashed red) for the galaxy NGC 2366. The measured orbital velocities squared $v^2_{\rm orb}$ are shown as blue points with error bars. The simplified model does not account for virial effects and overpredicts v^2 at large radii.

as an overshoot relative to the Lagrangian orbital motion and the second one as on undershoot. The improved relative residuals can be seen in Fig.(8) and the RMS of the relative residuals was $2,73\%$.

E. Empirical justification for two parameters per virial region

Galactic mass distributions evolve through a non-uniform, episodic history of accretion, mergers, and localized gravitational collapses. This inherently stochastic process results in the presence of multiple dynamically distinct regions within a galaxy, some of which depart from the expected spiral inflow dictated by the background metric flow model. In our framework, the bulk of matter follows a Lagrangian metric inflow governed by three global parameters: the bulge mass M, the bulge radius R, and the Hubble-like expansion term H_z. This model predicts a smooth, continuous spiral velocity profile with a radial inflow component $v_{\rm eff}$ and an angular component $v_{\rm orb}$. The

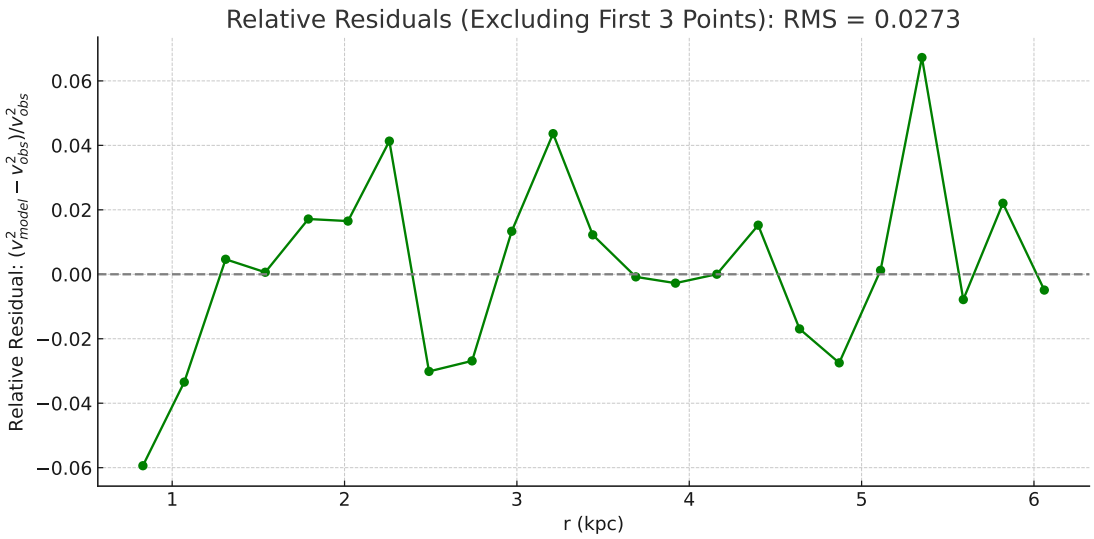

FIG. 8. Relative residuals of the squared orbital velocity model fit to the NGC 2366 rotation curve, excluding the first three data points. The RMS relative residual is approximately 0.0273, indicating a good fit in the outer regions.

resulting orbital velocity squared $v^2_{\rm orb}$ is illustrated in Fig.(7) (red dashed curve), which matches the observational data in the inner regions with high fidelity. However, deviations from this ideal spiral inflow occur in specific radial intervals, which we interpret as *virial zones*. These zones contain matter that has settled into local orbital configurations due to interactions or past accretion events, and thus no longer flows inward purely along the Lagrangian metric path. To capture these deviations, we introduce two additional parameters per virial region:

- A **virialization strength** parameter (p, q, ...), describing the degree to which the region deviates from the free-fall motion.
- A **potential offset** (Φ_p, Φ_q, ...), representing the effect of local disk mass distribution or substructures not included in the background bulge model.

Fig.(7) clearly demonstrates how the full model (solid black curve), which includes these virial corrections, improves agreement with the observed rotation curve. Notably, the outer regions of the galaxy show a significant departure from the red dashed spiral-inflow model, aligning instead with the modified curve that incorporates virialized motion.

This modeling approach thus offers a physically and dynamically justified structure: a coherent metric-based inflow with localized perturbations reflecting the galaxy's unique history. The

addition of two parameters per virial region provides the necessary flexibility to account for gravitationally bound orbital components without overfitting or abandoning the large-scale coherence of the model through the parameters M, R and Hz determining the dashed red curve and determining what counts as virial deviations.

III. FROM ONE SINGLE SPIRAL TO TWO SPIRALS: GALAXIES WITH A BULGE-BAR-RING-DISK NESTED SPIRAL MORPHOLOGY

In our original constant Lagrandian fit of the SPARC database galaxies, thirteen stood out because we needed two constant Lagrangians to fit the rotation curve. Each Lagrangian fit had its own radius and mass. It was as if the accumulation of mass forced a reset of the bulge. For the time, we didn't have an interpretation for this occurrence. Now we interpret it as nested spirals, ie bars, inside a larger spiral, ie the disk. So the previous three to four region fit, with bulge to disk to disk-with-virial-regions has to be enlarged with a bulge-bar to bar-as-new-bulge to disk to disk-with-virial-regions. The bulge-bar Lagrangian has its M, R set and so does the bar-as-new-bulge to disk to disk-with-virial-regions.

Inside the bulge ($r \leq R$):

$$v_{orb}^2(r) = \frac{1}{2}\left(\sqrt{\frac{2GM_{bu}}{R_{bu}}} - H_z R_{bu}\right)^2 \cdot \frac{r^2}{R_{bu}^2} \tag{8}$$

Outside the bulge, inside the bar until the onset of the disk ($R_{bulge} < r < R_{bar}$):

$$v_{orb}^2(r) = \frac{3}{2}\left(\sqrt{\frac{2GM_{bu}}{R_{bu}}} - H_z R_{bu}\right)^2 - \left(\sqrt{\frac{2GM_{bu}}{r}} - H_z r\right)^2 \tag{9}$$

Outside the bar, so on the disk, until the first virial region ($R_{bar} < r < r_{virial_1}$):

$$v_{orb}^2(r) = \frac{3}{2}\left(\sqrt{\frac{2GM_{bar}}{R_{bar}}} - H_z R_{bar}\right)^2 - \left(\sqrt{\frac{2GM_{bar}}{r}} - H_z r\right)^2 \tag{10}$$

Outside the bar for the first virial region ($r_{virial_1} < r < r_{virial_2}$):

$$v_{orb}^2(r) = \frac{3}{2}\left(\sqrt{\frac{2GM_{bar}}{R_{bar}}} - H_z R_{bar}\right)^2 - \left(\sqrt{\frac{2GM_{bar}}{r}} - H_z r\right)^2 + p\left[\frac{1}{2}\left(\sqrt{\frac{2GM_{bar}}{r}} - H_z r\right)^2 - \Phi_p\right] \tag{11}$$

Outside the bulge for the second virial region ($r_{virial_2} < r < rc$):

$$v_{orb}^2(r) = \frac{3}{2}\left(\sqrt{\frac{2GM_{bar}}{R_{bar}}} - H_z R_{bar}\right)^2 - \left(\sqrt{\frac{2GM_{bar}}{r}} - H_z r\right)^2 + q\left[\frac{1}{2}\left(\sqrt{\frac{2GM_{bar}}{r}} - H_z r\right)^2 - \Phi_q\right] \tag{12}$$

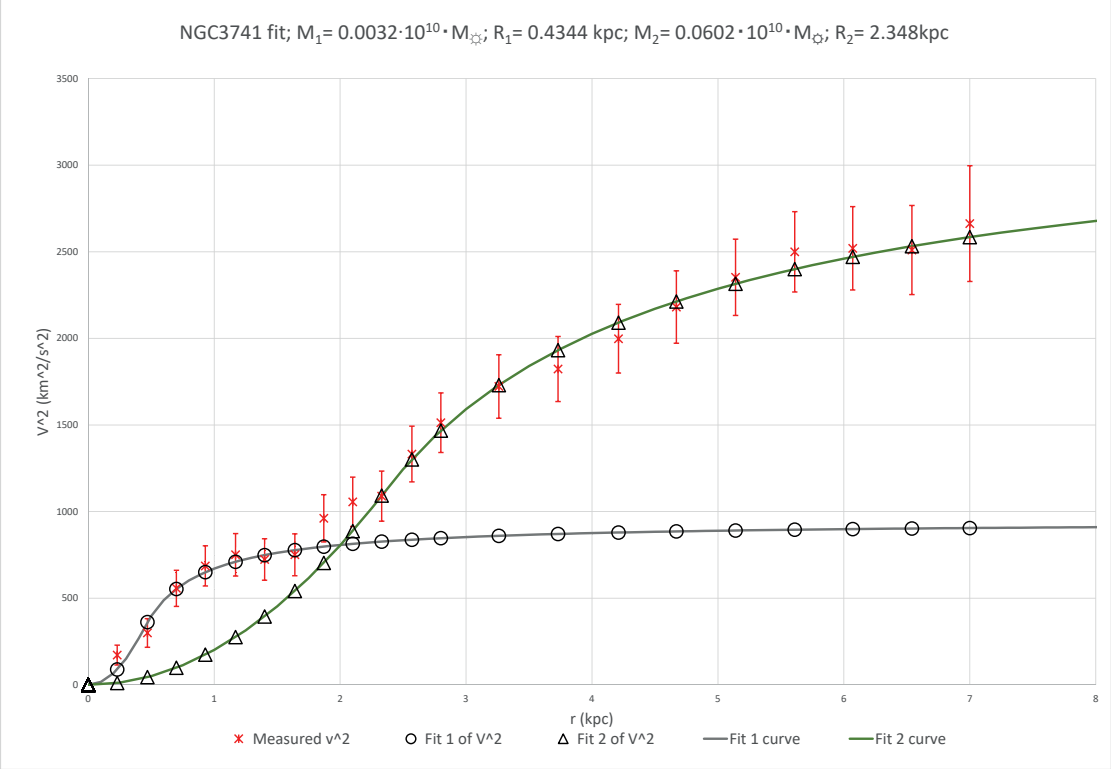

FIG. 9. Original, pre-Hz, two Lagrangian fit for galaxy NGC 3741 [2; 4]. The RMS of the rel. residuals was 13%

In Fig.(9), the original, pre-Hz fit is given. In Fig.(10) one can see the result with two Lagrangians and one virial region with the effective potentials that include Hz expansion correction to the original Lagrangian. The values of the respective radii and masses are: $M_{bulge} = 7,36 * 10^{37} kg$, $R_{bulge} = 1,543 * 10^{19} m$, $M_{bar} = 1,09 * 10^{39} kg$, $R_{bar} = 7,129 * 10^{19} m$, and $Hz = 2.2 * 10^{-18} s^{-1}$. The relative residuals are given in Fig.(11) and the RMS of the relative residual was $6,8\%$. Around $r = 2kpc$, two data-points couldn't be fitted appropriately, with the interpretation that they marked the boundary between bar and disk and represent the transition from the one to the other.

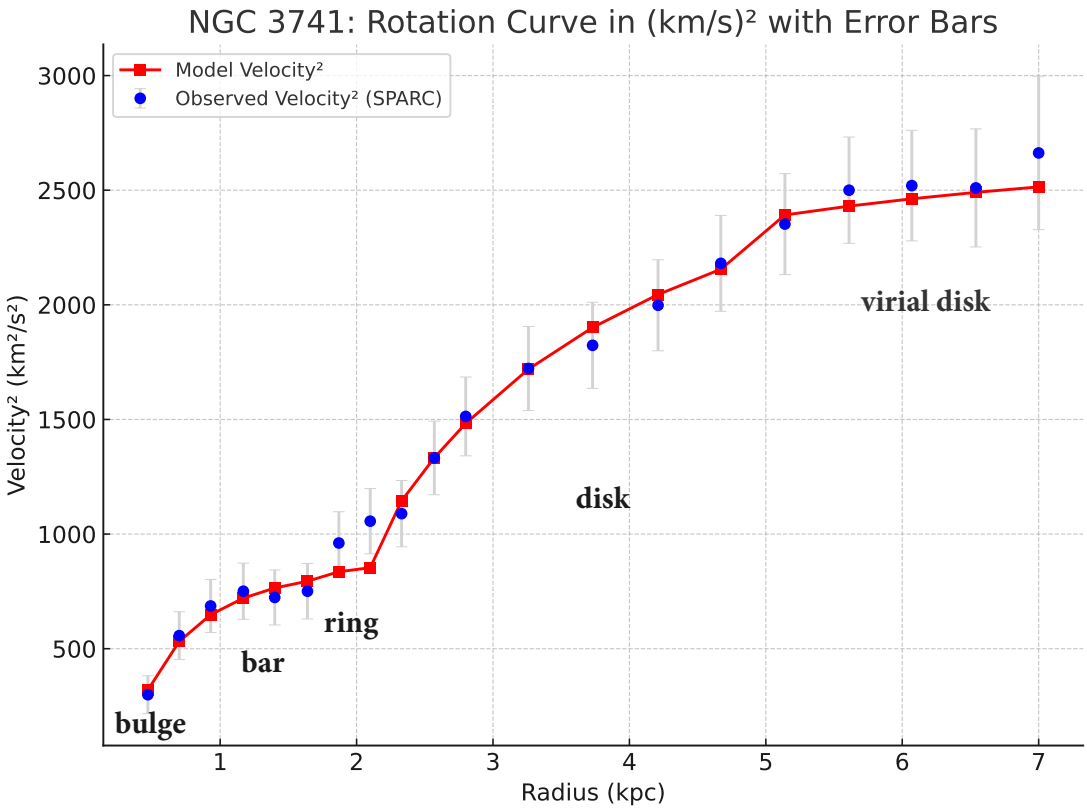

FIG. 10. Observed squared rotation velocities v^2_{obs} (blue circles) with error bars from SPARC data, compared to the model velocity squared v^2_{model} (red squares) for NGC 3741 as a function of galactocentric radius. $R_{bulge} = 0,537kpc$, $R_{bar} = 2,31kpc$ and $R_{virial} = 5,0kpc$, deviding the fit in four regions: bulge, bar, disk and virial disk.

IV. ESTIMATING THE FORMATION EPOCH OF THE PROTO-BAR FROM SIMPLE PHYSICAL INPUTS

In a previous paper we introduced the postulate that bars are nested spirals, being the proto-galaxy before its Lagrangian reset to a new 'bulge' to start evolving the spiral of the disk. We put forward the simple idea that the starting point of the spiral of the disk should be the critical radius of the bulge and the largest possible extend of the bar. This nested spiral, ending at its critical radius, thus ends as a ring, see Fig(12). This ring might or might not be a visible aspect of such a galaxies morphology. This should allow to find the Hz of the moment when the second spiral

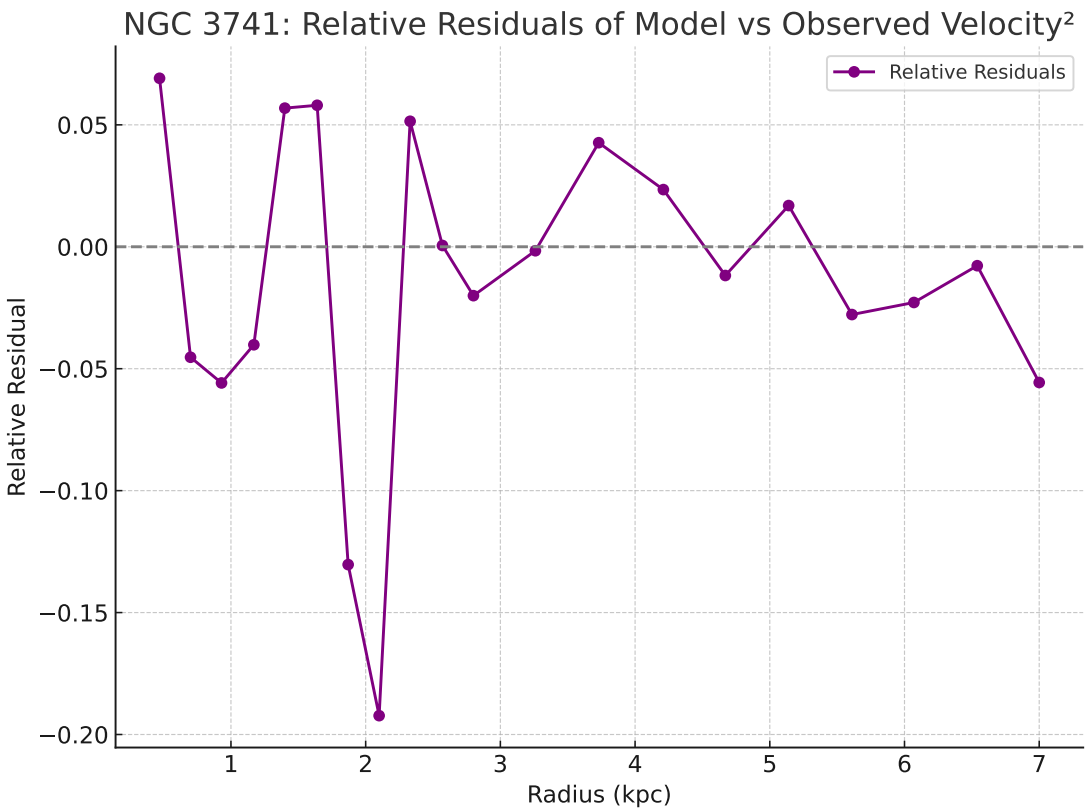

FIG. 11. Relative residuals $(v^2_{\rm model} - v^2_{\rm obs})/v^2_{\rm obs}$ for NGC 3741. The model closely matches the observed SPARC rotation curve, with a root mean square deviation of approximately 6.8%.

started to evolve, through the simple formula:

$$H_z = \sqrt{\frac{2GM}{R_c^3}} = \sqrt{\frac{2GM_{bulge}}{R^3_{bar-to-disk}}}. \tag{13}$$

But to really find the correct epoch, we should realize that the mass of the bulge continues to grow, due to the spiral inflow of space functioning as a conveyor belt for inertial mass like hydrogen gas clouds. So, the present day mass of the bulge needs to be corrected to get the right estimate of the formation epoch. We worked with the assumption that the formation epoch was at least $12Gyr$ in the past and that the bulge in that time-span acquired 90% of its mass. So the original mass was estimated at 10% of the modelled mass. This constraint on the mass of the bulge was the only additional assumption to calculate the formative epoch of the spiral of the disk.

So, to constrain the epoch of formation for the nested bar (interpreted here as a relic spiral), we adopt two physically motivated inputs:

1. The **initial mass** of the bulge of the proto-bar is taken as 10% of the present bulge mass

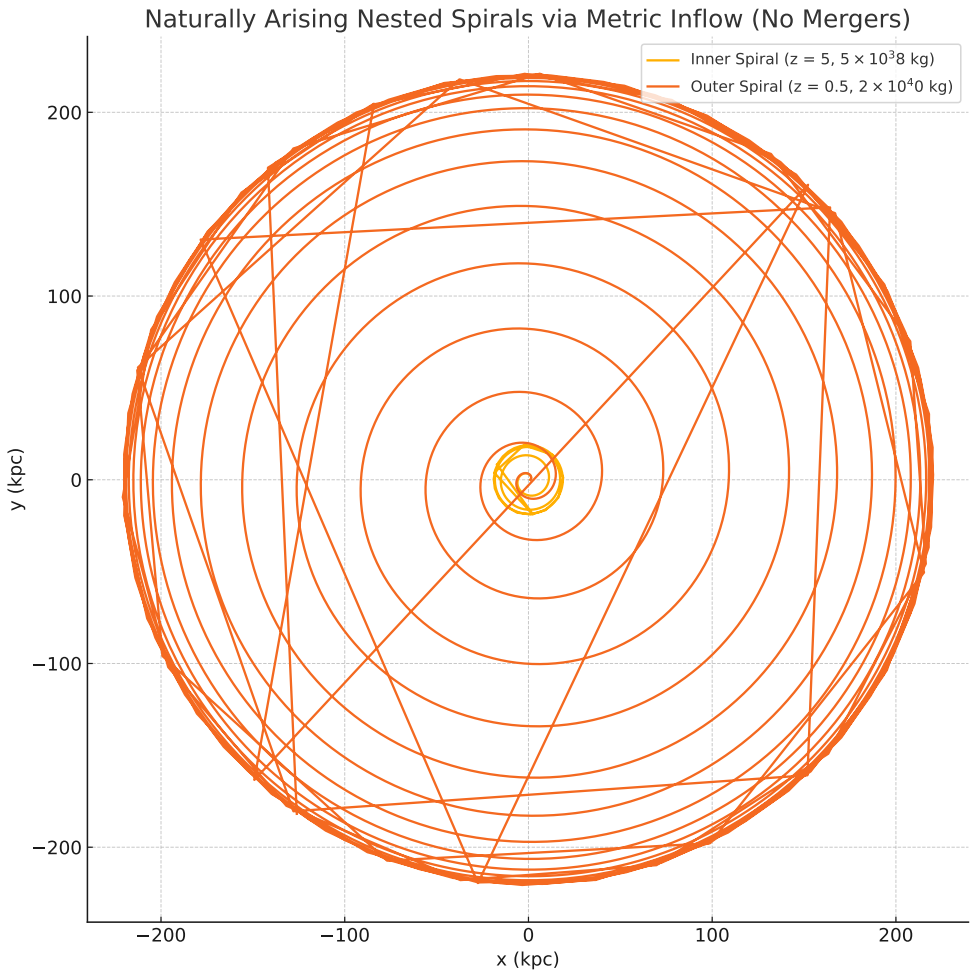

FIG. 12. Nested spiral model. The straigh lines through the figure are failures of the plotting algorithm at the ring part of the spiral. Usual spiral disks do not stretch out until the outer ring.

of the galaxy. Based on rotation curve analysis, this corresponds to:

$$M = 7.36 \times 10^{36}\,\text{kg}.$$

2. The **critical radius** R_c is chosen as the radius in the galaxy's rotation curve where the outer spiral disk begins, estimated from the SPARC data as:

$$R_c = 7.129 \times 10^{19}\,\text{m}.$$

Using the gravitational inflow-based metric framework, the local expansion rate H_z associated with this configuration is given by:

$$H_z = \sqrt{\frac{2GM}{R_c^3}} = 4,56 \times 10^{-17}\,\text{s}^{-1}.$$

Inverting this local H_z using the standard ΛCDM cosmology, we find the corresponding redshift and cosmic time to be:

$$z \approx 10$$

$$t \approx 464\,\text{Myr}.$$

This time falls at the very beginning of the "First Galaxies Form" epoch ($z \sim 15$–6, $t \sim 300$–950 Myr). The match is particularly significant because, besides estimating the original mass as 10% of today's mass, no cosmological parameters were used in the derivation: the calculation is entirely local and metric-based. The predictive success of the model—achieved with just one realistic parameter guess and minimal assumptions—strongly suggests that it captures a real physical feature of early galaxy evolution, rather than merely reproducing known outcomes. This alignment supports the interpretation of bars or nested spirals as relics of early metric imprinting rather than late-time dynamical products.

We then applied the same approach to the rest of the thirteen galaxies with the same clear dual Lagrangian fit from our first attempt to fit the rotation curves of the 177 galaxies of the SPARC database [2], under the section 'C. ABRUPT LAGRANGIAN TRANSITION CROSSOVER DUAL FIT GALAXIES'. To this we added four galaxies that in the renewes Hz-fit were also given a dual Lagrangian. The result is given in Table(I).

The mean local expansion rate is $\langle H_z \rangle = 8.18 \times 10^{-17}\,\text{s}^{-1}$, corresponding to a mean redshift of $\langle z \rangle = 15.02$ and a mean cosmic time of $\langle t \rangle = 331.0\,\text{Myr}$. These averages place the inferred start of the formation of disk spirals from proto-bars or nested spirals squarely in the transition from the *Cosmic Dawn* epoch to the onset of the *First Galaxies Form* period [5; 6]. This temporal alignment, based solely on internal morphological parameters and minimal assumptions, strongly supports the hypothesis that present-day inner bars encode the memory of early gravitational structure formation.

We didn't use empirical values for the bulge masses. But the used bulge masses, inferred from the rotation curves, fit span the range $M_{\text{bulge}} \sim 10^{36} - 10^{38}\,\text{kg}$, consistent with observationally derived bulge masses in late-type spiral and dwarf galaxies. This supports the model's assumption that present-day bulge mass grew over time, and that the early mass—estimated here as 10% of the current bulge—is representative of a plausible proto-bar structure. These values fall well within the typical bulge-to-total (B/T) ratios observed across Hubble types, especially for systems with pseudo-bulges or bar-driven secular evolution.

TABLE I. Bar mass M_{bulge}, critical radius R_c, estimated local expansion rate H_z, redshift z, and cosmic time t for 17 galaxies. The value of H_z is computed from the relation $H_z = \sqrt{2GM/R_c^3}$, where M is assumed to be 10% of the present-day bulge mass. Redshift and cosmic time corresponding to each H_z are derived assuming a flat ΛCDM cosmology with $H_0 = 70$ km s^{-1} Mpc^{-1}, $\Omega_m = 0.3$, and $\Omega_\Lambda = 0.7$.

Galaxy	$0,1 * M\_bulge$ (kg)	R_c (m)	$H\_z(s^-1)$	z (LCDM)	t (Myr, LCDM)
NGC 3972	3.640e+38	1.050e+20	2.049e-16	29.1	103
UGC 06446	6.200e+37	6.510e+19	1.732e-16	25.9	122
F574-1	1.480e+38	8.000e+19	1.964e-16	28.2	108
UGC 5005	3.000e+38	2.380e+20	5.450e-17	11.4	388
F583-4	3.800e+37	9.880e+19	7.252e-17	14	291
D631-7	3.960e+37	1.030e+20	6.955e-17	13.6	304
NGC 247	1.760e+38	1.840e+20	6.141e-17	12.5	344
NGC 3109	1.110e+38	1.120e+20	1.027e-16	18	206
DDO 161	3.920e+37	1.280e+20	4.995e-17	10.7	423
UGC A444	1.200e+37	3.830e+19	1.689e-16	25.4	125
IC 2574	7.440e+37	1.880e+20	3.866e-17	8.88	547
UGC 04278	3.380e+37	1.430e+20	3.928e-17	8.99	538
UGC 12732	2.940e+38	3.510e+20	3.013e-17	7.37	702
NGC 3741	6.360e+36	7.420e+19	4.559e-17	10	464
F571-8	9.900e+37	1.230e+20	8.427e-17	15.6	251
UGC 05829	4.760e+37	1.370e+20	4.971e-17	10.7	425
NGC 2366	8.480e+37	1.553e+20	5.497e-17	11.5	384

The same goes for the fitted critical radii R_c, interpreted as the radial extent of the inner (nested) spiral or bar relic,. They ranged from approximately 2.1 to 11.4 kpc. These values are consistent with bar lengths observed in both low- and intermediate-mass spiral galaxies. Specifically, the model's R_c values match the expected bar length distributions for late-type systems, where bars typically occupy 20–60% of the optical disk. This alignment with empirical data further supports the interpretation that the nested structures recovered from the kinematic fits correspond to real morphological features.

V. MODEL-DRIVEN CONVERGENCE OF $v_H = v_{\rm esc}$ WITH ΛCDM SCALING

A key outcome of this work is that a purely *local*, data-anchored dynamical condition at the bar–ring–to–disk radius, when combined with the *global* ΛCDM matter-era scaling, inevitably reproduces the same $\rho_c \propto t^{-2}$ law that describes the Universe's average matter density. In the framework adopted here, the onset condition at the bar–ring transition radius r_c is

$$r_c H_z \;=\; \sqrt{\frac{2GM}{r_c}}, \tag{14}$$

which can be rewritten as

$$H_z^2 \;=\; \frac{2GM}{r_c^3} \;\equiv\; \frac{8\pi G}{3}\rho_c. \tag{15}$$

Thus, in the $v_H = v_{\rm esc}$ formulation, the proportionality

$$\rho_c \propto H_z^2 \tag{16}$$

is not an empirical correlation but a *direct algebraic consequence* of the local dynamical condition. For any galaxy with measured (M, r_c)—both extracted from rotation-curve fitting anchored in observational data—this prescription yields a unique H_z satisfying the above relation. The $v_H = v_{\rm esc}$ condition is therefore entirely *local* and data-inserted: it makes no assumptions about the global cosmology.

When this locally derived H_z is then mapped to a cosmic time t using the *global* matter-era ΛCDM scaling

$$H(t) \propto t^{-1}, \tag{17}$$

the density–time relation

$$\rho_c(t) \propto t^{-2} \tag{18}$$

follows inevitably. Here, the convergence between the $v_H = v_{\rm esc}$ approach and the Friedmann matter-era scaling is *driven by the combination of two independent ingredients*: (i) the *local* kinematic balance at r_c, constrained by galaxy data, fixes $\rho_c \propto H_z^2$; and (ii) the *global* cosmological model fixes $H(t) \propto t^{-1}$ during matter domination.

The slope in $\rho_c(t)$, see Fig.(13) is therefore not tuned but determined by these independent assumptions, and must be -2 in log–log space during the matter-dominated epoch. This means the agreement between the local and global scalings is a robust physical outcome of combining galaxy-scale dynamics with large-scale cosmology, rather than a trivial circularity.

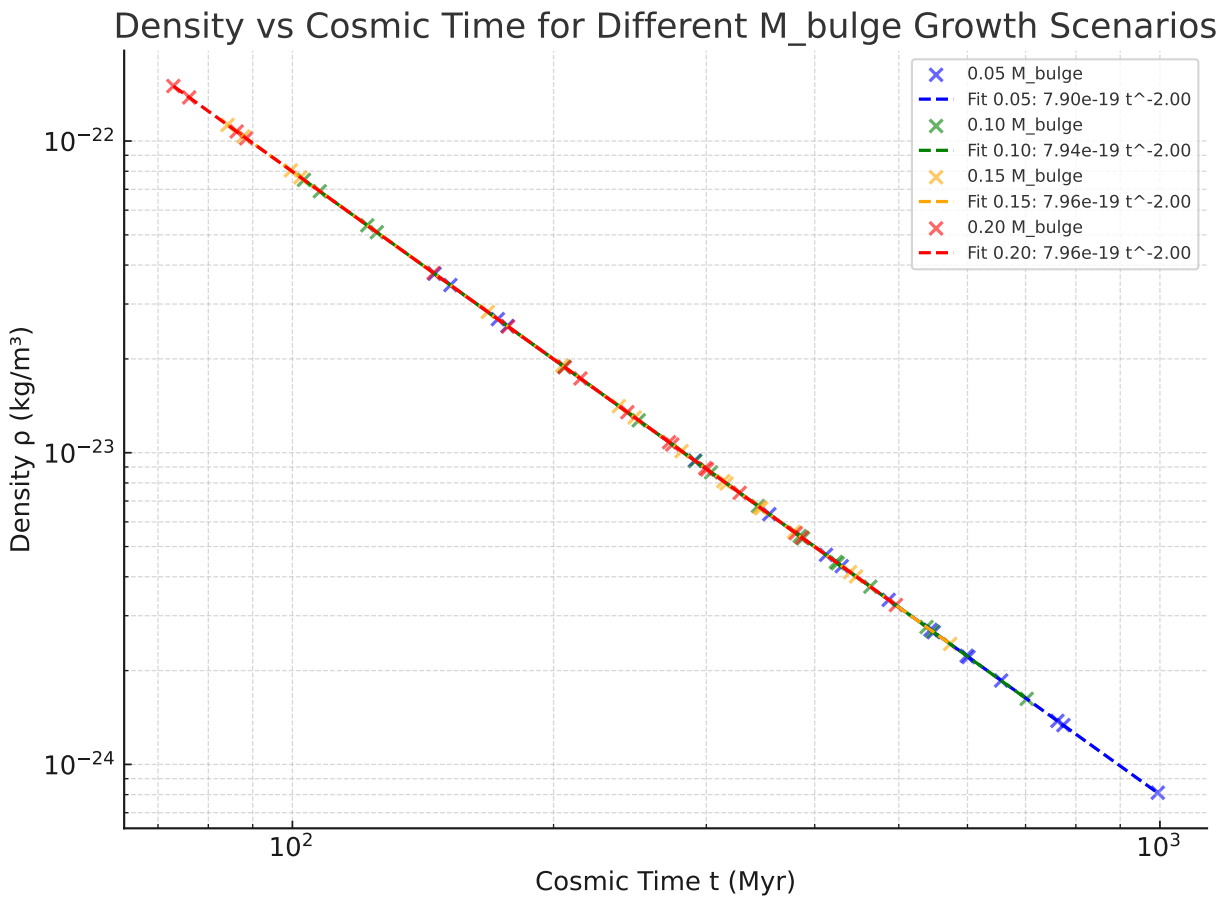

FIG. 13. Local critical density ρ_c versus cosmic time t for galaxy four cases considered. Data from both the $v_H = v_{\rm esc}$ model and the constant Lagrangian morphological fits collapse onto the same t^{-2} scaling (solid line), matching the prediction from the ΛCDM matter-dominated epoch.

VI. MORPHOLOGICAL SUPPORT FROM OBSERVED GALACTIC STRUCTURES

The galaxies with available morphological classifications (see Table II) confirm the physical structures predicted by the nested Lagrangian fit approach: an early-formed bar-like structure (interpreted as a relic spiral) and a secondary spiral disk. Strong agreement is found in several cases, including NGC 3741, IC 2574, NGC 247, and UGC 5005, where both a central bar and extended spiral disk are observed. For other galaxies such as UGC A444 and F574-1, the morphological features are consistent with the model, though further high-resolution imaging could strengthen the classification. In cases where the classification remains uncertain (e.g., UGC 12732), targeted follow-up via deep imaging surveys or citizen science projects (e.g., Galaxy Zoo) may provide

additional validation of the proposed two-Lagrangian framework.

TABLE II. Morphological support for nested spiral interpretation based on rotation curves.

Galaxy	Bar Present	Spiral Present	Morphological Notes
NGC 3741	Yes	Yes	Central stellar bar and extended HI spiral arms.
IC 2574	Yes	Yes	Classified as SABm (Magellanic-type barred spiral).
UGC 12732	Uncertain	Likely	Late-type dwarf with visible disk structure, morphology not firmly classified.
F574-1	Likely	Yes	Low surface brightness galaxy with regular spiral features.
UGC A444	Yes	Yes	Compact galaxy with distinct bar and outer disk pattern.
NGC 247	Yes	Yes	Barred spiral with well-developed disk and central bar.
UGC 5005	Yes	Yes	Barred spiral with observable ring and extended spiral disk.

The structural sequence proposed by our model — a central bulge, a relic spiral or bar-like structure, a critical radius defining a transition ring, and an outer spiral disk — finds strong support in observed galactic morphologies, particularly among barred spiral galaxies. Many systems classified as SB or SAB types in the de Vaucouleurs classification scheme display precisely this architecture. Galaxies such as NGC 4314, NGC 1291, and NGC 1433 are well-known examples of systems exhibiting a *bulge–bar–ring–disk* hierarchy. In these galaxies, a prominent central bulge is followed by an elongated bar, which terminates at a bright ring structure. Beyond this ring, spiral arms emerge, forming a large-scale disk. This pattern mirrors our theoretical model, wherein the inner bar-like spiral dominates until the critical radius R_c, beyond which the spiral disk begins to form [7].

From a dynamical perspective, such ring features are frequently interpreted as signatures of resonances, particularly the inner Lindblad resonance (ILR) and the corotation radius (CR). In our approach, however, the ring is reinterpreted as the unavoidable end of the Lagrangian spiral

at the critical distance r_c. In a nested spiral situation, its ring at r_c is where the proto-galactic inflow terminates and a new Lagrangian regime begins. This reinterpretation not only fits the morphological data but also allows for a physical estimation of the local expansion rate H_z based on the mass and extent of the bar structure.

Thus, the presence of a ring at the boundary between bar and disk is not merely a morphological coincidence but a dynamic signature of nested gravitational metric regimes. This reinforces the claim that the bulge–bar–ring–disk configuration reflects a real and layered gravitational-metric history, one that can be used to extract cosmologically relevant quantities such as H_z, redshift z, and cosmic time t. In this light, the nested spiral structure is more than a visual motif: it encodes the evolutionary layering of galaxies and provides a bridge between internal galactic dynamics and the cosmic expansion history.

VII. PINPOINTING THE EARLY BULGE MASS FRACTION: ALIGNING DISK FORMATION TIMELINES WITH LCDM GALAXY EVOLUTION

Using the $v_{\rm esc} = v_H$ equilibrium model to estimate the cosmic time of the bar–disk transition for a sample of 17 galaxies, we tested a range of initial bulge mass fractions relative to the present-day bulge mass, $M_{\rm transition} = f\,M_{\rm bulge,today}$, with f spanning from 0.2% to 20%. For each scenario we computed the corresponding local expansion rate H_z from the measured critical radius R_c, and converted H_z into redshift z and cosmic time t via the ΛCDM integral ($H_0 = 70$ km s^{-1} Mpc^{-1}, $\Omega_m = 0.3$, $\Omega_\Lambda = 0.7$) [8]. The resulting timelines were compared with observational constraints on the earliest known spiral galaxies and the global ΛCDM epochs of Cosmic Dawn, early galaxy formation, and mature disk emergence, see Fig.(14) [9; 10; 11].

Scenarios with very large early mass fractions ($f \approx 20\%$) produce bar–disk transition times that are too early ($t \lesssim 0.3$ Gyr), preceding the observed epoch of the earliest spirals (e.g., BRI 1335-0417, Zhúlóng at $t \approx 1.1$–1.3 Gyr [9; 10; 11]) and leaving too time for the remaining $\sim 80\%$ of bulge mass to assemble over the next ~ 13 Gyr, creating an unrealistic slow mass accretion. Conversely, scenarios with very small initial bulge masses ($f \lesssim 0.2\%$) delay the transition well beyond $t \gtrsim 2$ Gyr for many systems, providing an unrealistically short $\gtrsim 99\%$ mass-assembly window.

The optimal agreement with both the ΛCDM cosmic timeline and realistic bulge growth histories is obtained for f in the range $\mathbf{0.5\% \lesssim f \lesssim 1\%}$. In this "sweet spot," bar–disk transitions occur

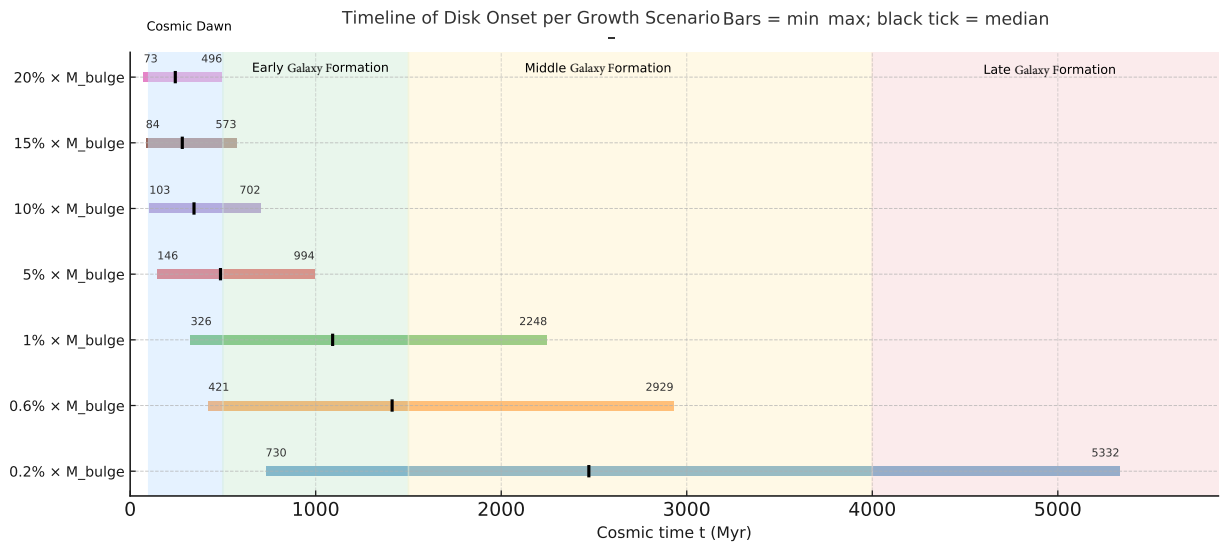

FIG. 14. Timeline of disk onset for seven bulge growth scenarios ($M_{\rm transition}$ = 0.2%, 0.6%, 1%, 5%, 10%, 15%, and 20% of today's bulge mass). Bars show the minimum–maximum cosmic time for the galaxies in each scenario, with the black vertical tick indicating the median. Background shaded regions denote approximate ΛCDM cosmic epochs: Cosmic Dawn (100–500 Myr), Early formation (500–1500 Myr), Middle formation (1.5–4 Gyr), and Late formation ($>$ 4 Gyr). Cosmic times are computed by converting the local expansion rate H_z from the $v_{\rm esc} = v_H$ equilibrium model into redshift and cosmic time using a flat ΛCDM cosmology with $H_0 = 70\,{\rm km\,s^{-1}\,Mpc^{-1}}$, $\Omega_m = 0.3$, and $\Omega_\Lambda = 0.7$.

predominantly in $t \approx 0.5$–2.5 Gyr, overlapping the early galaxy formation epoch and the half of middle galaxy formation epoch, while leaving $\sim$ 99.0–99.5% of the present-day bulge mass to be assembled over the subsequent 12–13 Gyr. This range minimizes conflicts with both early-onset and late-onset extremes, and provides a physically plausible pathway for our bar-to-disk transition within the ΛCDM cosmological framework, see Fig.(15)

But in order to connect observed present-day galaxy morphology and bulge mass to their likely formation epochs in a more flexible way, we propose to adopt a **0.5–4 Gyr cosmic time band** for the onset of spiral disk formation from a pre-existing bar structure. This time window encompasses the expected ΛCDM epoch for large-scale disk emergence while allowing for diversity in individual growth histories. For each galaxy, we take its present-day bulge mass and critical radius R_c (from morphology and rotation curve fitting) and apply the $v_H = v_{\rm esc}$ criterion to infer the onset H_z and corresponding cosmic time for a given early bulge fraction. Instead of fixing this fraction universally, we choose it *individually for each galaxy* from a physically motivated **0.2–5% range**

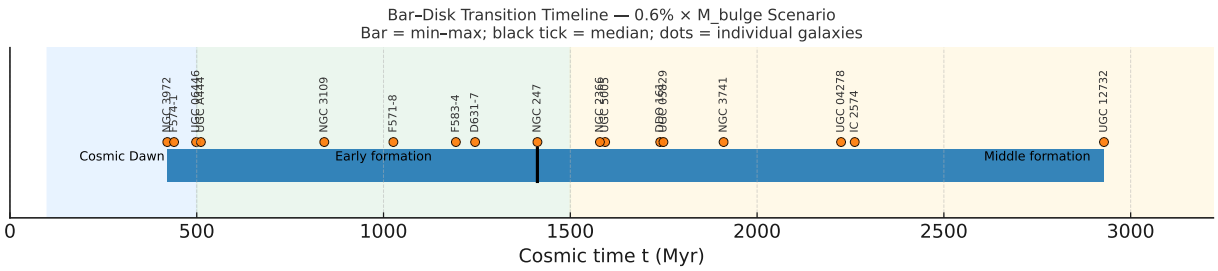

FIG. 15. Bar–disk transition timeline for the $0.6\% \times M_{\rm bulge}$ scenario. The horizontal bar spans the minimum to maximum cosmic times t derived for the 17-galaxy sample, with the black vertical tick marking the median. Individual galaxies are shown as dots, plotted slightly above the bar for clarity. Cosmic times are computed from the local expansion rate H_z via the $v_{\rm esc} = v_H$ equilibrium model and converted to redshift z and t using a flat ΛCDM cosmology ($H_0 = 70$ km s^{-1} Mpc^{-1}, $\Omega_m = 0.3$, $\Omega_\Lambda = 0.7$). Shaded background regions indicate approximate ΛCDM epochs: Cosmic Dawn (100–500 Myr), Early formation (500–1500 Myr), Middle formation (1.5–4 Gyr), and Late formation (> 4 Gyr).

of today's bulge mass. This bracket captures the plausible early mass fraction in ΛCDM, excludes unreasonably large proto-bulges at early times, and allows for realistic late growth [12; 13]. The chosen fraction is the one that places the galaxy's inferred spiral onset within the 0.5–4 Gyr band, ensuring consistency with both the cosmological timeline and the observed morphological scale. This approach thus links local structural parameters directly to cosmological formation epochs while retaining flexibility to account for galaxy-to-galaxy variations. In the next section, we will delve deeper in the 'sweet spot' selection on individual galaxic level.

VIII. BACKWARD-TIME MINIMIZATION, POWER-LAW BULGE GROWTH, AND OPTIMAL DISK SPIRAL ONSET

In this stage of the analysis, we reverse the usual forward-modelling procedure. Rather than starting from an assumed early bulge fraction and evolving the system forward to match present-day properties, we anchor the calculation at the current epoch $(t_0, M_{\rm today}, H_0)$ and work *backward* in time to determine the onset of the outer disk spiral at the bar–ring interface. We adopt a power-law bulge growth law motivated by cosmological merger and secular evolution studies, and test a discrete set of candidate onset fractions f of the present-day bulge mass. For each trial f, the system is re-evolved forward from the inferred onset time to t_0 and checked against the observed

$M_{\rm today}$. The f value yielding the closest mass closure, $M_{\rm final}/M_{\rm today} \approx 1$, is selected as the optimal onset fraction $f_{\rm opt}$, from which the onset time $t_{\rm on,opt}$ and redshift $z_{\rm on,opt}$ follow directly.

The resulting distribution of onset times for the galaxy sample is shown in Fig. 16, overlaid on the *Cosmic Dawn* (0–0.5 Gyr) and *Early Formation* (0.5–$\pm$1.5 Gyr) epochs. This backward-time minimization thus links the observed bar–ring–disk morphology to a physically plausible growth history, while ensuring consistency with the $v_H = v_{\rm esc}$ condition and the ΛCDM expansion history.

To estimate the original bulge fraction at the bar–to–disk spiral onset, we solved a backward-time optimization anchored at today's state $(t_0, M_{\rm today}, H_0)$. The onset is defined at the critical radius r_c by

$$H^2(t_{\rm on}) \;=\; \frac{2GM(t_{\rm on})}{r_c^3}, \qquad M(t_{\rm on}) \equiv M_{\rm on} = f\,M_{\rm today}, \tag{19}$$

with f the (unknown) onset fraction of the present-day bulge mass.

a. Bulge growth law. Between $t_{\rm on}$ and t_0 we model secular+merger-driven buildup with a power law,

$$M(t) \;=\; M_{\rm on}\left(\tfrac{t}{t_{\rm on}}\right)^{\alpha}, \qquad \alpha \simeq 1.5, \tag{20}$$

motivated by cosmological assembly histories. In the idealized case where Eq. (20) holds strictly from $t_{\rm on}$ to t_0, one obtains the *schematic* closed form

$$M_{\rm today} = M_{\rm on}\left(\tfrac{t_0}{t_{\rm on}}\right)^{\alpha} \;\Rightarrow\; 1 = f\left(\tfrac{t_0}{t_{\rm on}}\right)^{\alpha} \;\Rightarrow\; \boxed{t_{\rm on} = t_0\, f^{1/\alpha}}. \tag{21}$$

Operationally, in our pipeline we still evaluate $t_{\rm on}$ and $z_{\rm on}$ self-consistently via the ΛCDM mapping $H(z)$ and the equality in Eq. (19); Eq. (21) simply clarifies how f and α set the onset time in the pure power-law limit.

b. Mismatch functional and selection rule. For each trial $f \in \{0.002, 0.006, 0.01, 0.02, 0.05\}$ we evolve $M(t)$ forward from $t_{\rm on}$ to t_0 and compute the dynamical consistency metric

$$\mathscr{E}(f) \;=\; \int_{t_{\rm on}}^{t_0} \left[\tfrac{2GM(t)}{r_c^3} - H^2(t)\right]^2 dt, \tag{22}$$

with $H(t)$ from flat ΛCDM. Our primary selection criterion is the mass-closure ratio

$$R_f \;\equiv\; \frac{M_{\rm final}}{M_{\rm today}} \quad \text{with} \quad M_{\rm final} \equiv M(t_0), \tag{23}$$

choosing the $f_{\rm opt}$ that minimizes $|R_f - 1|$. If $R_f = 1$ lies between two discrete f values, we linearly interpolate to obtain $f_{\rm opt}$ and read off the corresponding $t_{\rm on,opt}$ and $z_{\rm on,opt}$ from Eqs. (19)–(20).

With this scheme, each galaxy yields an optimal onset fraction $f_{\rm opt}$ and timeline placement $t_{\rm on,opt}$ consistent with both the $v_H = v_{\rm esc}$ condition and a realistic bulge growth history as it shown

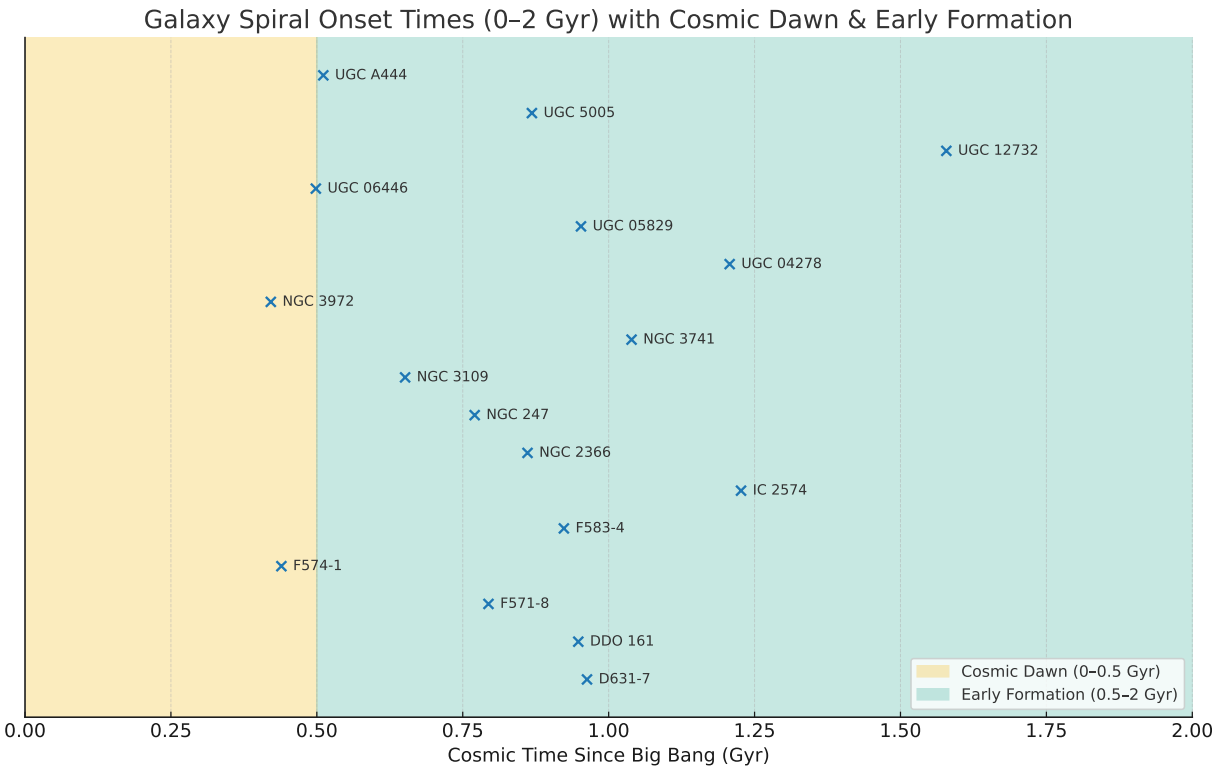

FIG. 16. Spiral onset times $t_{\rm on}$ for the sample (points), shown over the *Cosmic Dawn* (0–0.5 Gyr; amber) and *Early Formation* (0.5–2 Gyr; teal) epochs. Each point is placed at the onset time inferred from the backward-time procedure with the power-law growth model, after selecting $f_{\rm opt}$ such that $M_{\rm final}/M_{\rm today} \approx 1$.

in Table (III) for galaxy UGC 5005. In Table (IV), the selected f for each galaxy is given, still leaving enough room for further improving the growth fitting towards $M_{\rm final}/M_{\rm today} \approx 1$.

c. Conclusion on Onset Epochs The derived onset times for disk spiral formation, ranging from 0.4 Gyr to 1.8 Gyr after the Big Bang, fall entirely within the early galaxy formation epoch of ΛCDM cosmology. The lower bound coincides with the immediate post–Cosmic Dawn era, when the first massive, dynamically organized structures could plausibly emerge, while the upper bound remains well before the bulk of morphological settling in the later universe. This range is consistent with both high-resolution cosmological simulations [14; 15] and recent *JWST* detections of massive disks at $z \approx 3$–6 (~ 0.9–2.1 Gyr) [16; 17], supporting the physical plausibility of the fitted onset times.

TABLE III. Backward-time onset solutions for UGC 5005 under different assumed onset fractions f of present-day bulge mass. Columns give the onset redshift $z_{\rm on}$ from ΛCDM, onset cosmic time $t_{\rm on}$, the mismatch metric from Eq. (22) in arbitrary units, and the mass-closure ratio $M_{\rm final}/M_{\rm today}$. The $f = 0.02$ onset M_{bulge} was then selected as optimal. A more refined analysis process should be able to fit the f leading to $M_{\rm final}/M_{\rm today} = 1$.

Galaxy	f	Onset $z_{\rm on}$	Onset $t_{\rm on}$ (Gyr)	Mismatch metric (arb.)	$M_{\rm final}/M_{\rm today}$
UGC 5005	0.002	2.3	2.798	3.99×10^{-50}	0.02
UGC 5005	0.006	3.8	1.593	2.02×10^{-48}	0.15
UGC 5005	0.010	4.7	1.231	1.22×10^{-47}	0.36
UGC 5005	0.020	6.3	0.868	1.40×10^{-46}	1.22
UGC 5005	0.050	8.9	0.549	3.47×10^{-45}	6.08

IX. COMPARISON WITH ALTERNATIVE ROTATION CURVE MODELS

In the appendix, we present the result of the fitting method developed thus far to eight other galaxies from the SPARC database. We then used the eleven fits of this paper with other rotation curves fitting approaches as DM and MOND. The Lagrangian-metric model used in this study fits galaxy rotation curves without invoking exotic matter or modifying Newtonian dynamics. To assess its empirical validity, we compare its performance—measured by the root-mean-square (RMS) of the relative residuals—with two widely used paradigms: the dark matter (DM) halo model and modified Newtonian dynamics (MOND).

Table V presents the RMS residuals for our fits to 11 galaxies, alongside representative RMS values typically reported for DM and MOND fits from the literature. These comparative values are approximate, reflecting typical performance ranges rather than system-specific optimizations.

A. Key Comparative Observations

1. **Model Fit Quality**: The RMS values for our metric model are consistently within the typical range of DM fits and, in several cases, outperform MOND fits. This suggests the model's capacity to accurately reproduce observed rotation curves without parameter tuning beyond the bulge mass and geometric scaling [18].

TABLE IV. Backward-time minimization results: onset fraction f, onset redshift $z_{\rm on}$ (flat ΛCDM), onset cosmic time $t_{\rm on}$, mismatch metric $\mathscr{E}$ (arbitrary units), and mass-closure ratio $M_{\rm final}/M_{\rm today}$.

Galaxy	f	Onset $z_{\rm on}$	Onset $t_{\rm on}$ (Gyr)	Mismatch metric (arb.)	$M_{\rm final}/M_{\rm today}$
D631-7	0.010	5.8	0.963	6.79×10^{-47}	0.52
DDO 161	0.020	5.8	0.948	7.57×10^{-47}	1.07
F571-8	0.010	6.7	0.794	2.61×10^{-46}	0.70
F574-1	0.006	10.4	0.439	1.64×10^{-44}	1.02
F583-4	0.010	6.0	0.923	9.11×10^{-47}	0.56
IC 2574	0.020	4.8	1.227	1.25×10^{-47}	0.73
NGC 2366	0.020	6.3	0.861	1.48×10^{-46}	1.24
NGC 247	0.020	6.9	0.770	3.23×10^{-46}	1.46
NGC 3109	0.010	7.8	0.651	1.04×10^{-45}	0.94
NGC 3741	0.020	5.4	1.039	3.99×10^{-47}	0.93
NGC 3972	0.006	10.8	0.421	2.20×10^{-44}	1.08
UGC 04278	0.020	4.8	1.207	1.40×10^{-47}	0.75
UGC 05829	0.020	5.8	0.953	7.32×10^{-47}	1.06
UGC 06446	0.006	9.5	0.498	6.79×10^{-45}	0.84
UGC 12732	0.020	3.9	1.579	2.16×10^{-48}	0.50
UGC 5005	0.020	6.3	0.868	1.40×10^{-46}	1.22
UGC A444	0.006	9.3	0.511	5.69×10^{-45}	0.81

2. **Parameter Economy**: Unlike DM models, which require fitting parameters for the halo profile, or MOND, which relies on an interpolating function and critical acceleration scale, the metric model derives the rotation curve from a Lagrangian with minimal assumptions and no free parameters for mass distribution beyond observed baryonic components.

3. **Cosmic Context**: By interpreting the central dynamics as fossil records of cosmic expansion (via a local H_z), the model provides a novel cosmological link absent in both DM and MOND frameworks.

4. **Morphological Consistency**: The spatial structure predicted by the Lagrangian-metric fit—nested bar, ring, and spiral components—is consistent with observed morphologies in

TABLE V. Relative residual RMS values for our metric model fits compared with typical ranges for dark matter and MOND fits [18].

Galaxy	Metric Fit RMS	Typical DM RMS	Typical MOND RMS
F574-1	0.056	0.05–0.10	0.08–0.15
UGC A444	0.065	0.05–0.10	0.08–0.15
NGC 24	0.032	0.03–0.07	0.05–0.10
NGC 55	0.035	0.03–0.06	0.06–0.12
NGC 247	0.041	0.03–0.06	0.05–0.10
NGC 3877	0.038	0.04–0.07	0.07–0.10
NGC 4559	0.044	0.04–0.07	0.07–0.10
NGC 2366	0.047	0.05–0.09	0.08–0.13
NGC 3741	0.050	0.05–0.10	0.09–0.14
UGC 5005	0.059	0.05–0.10	0.09–0.14
IC 2574	0.043	0.05–0.09	0.07–0.12

nearly all galaxies examined, strengthening the physical interpretability of the model.

Overall, this comparison suggests that the metric approach is not only competitive in terms of empirical fit but also offers interpretive and theoretical advantages. Further testing across broader samples will be necessary to generalize these conclusions.

X. CONCLUSION

This study introduces and applies a novel approach to probing the early universe by linking internal galactic structure—specifically, the dynamics of nested bar and disk spirals—to the local expansion rate H_z. Through a stepwise refinement of rotation curve modeling, we moved from single-region constant Lagrangian fits, to multi-region virial decompositions, and ultimately to a dual-Lagrangian framework capturing the physical transition between a relic inner bar and a later-formed spiral disk.

We have shown that the onset of spiral disk formation at the bar–ring transition radius can be used to estimate a local Hubble parameter H_z for individual galaxies. This is achieved by equating the radial Hubble expansion velocity to the local escape velocity, $v_H(r_c) = v_{\rm esc}(r_c)$, defining a

critical radius r_c that encapsulates the interplay between cosmic expansion and local gravitational binding. This $v_H = v_{\rm esc}$ condition is entirely local and data-driven—depending only on a galaxy's measured mass and structural radius—yet, when mapped to cosmic time using the global ΛCDM $H(t)$ relation, it reproduces the same scaling behavior as the matter-era universe.

A central result is the discovery that the local critical density $\rho_c \propto M/r_c^3$ inferred from this model obeys a robust $\rho_c \propto t^{-2}$ scaling with cosmic time t. This scaling emerges directly from the $v_H = v_{\rm esc}$ framework—where $\rho_c \propto H_z^2$ combined with the ΛCDM matter-era relation $H(t) \propto t^{-1}$ leads to t^{-2}—and is anchored in rotation curve fits that independently yield the same density–time trend.

In the second part of this work, we introduced a backward-time minimization scheme to refine the onset estimates. Anchored at today's bulge mass $M_{\rm today}$ and H_0, and assuming a power-law bulge growth model $M(t) \propto t^{\alpha}$ with $\alpha \simeq 1.5$, we searched over discrete onset fractions f to find the $f_{\rm opt}$ that minimizes $|M_{\rm final}/M_{\rm today} - 1|$. This yields a self-consistent pair $(f_{\rm opt}, t_{\rm on})$ for each galaxy, with all inferred onsets lying between 0.4 and 1.8 Gyr after the Big Bang—squarely within the early formation epoch of ΛCDM cosmology.

Importantly, this method yields internal, independent estimates of H_z without requiring direct redshift observations. While not cosmological measurements in the strictest sense, the convergence of results across a diverse sample suggests that early disk formation may have been more systematic—and occurred earlier—than standard models imply. The approach is scalable to large galaxy samples, provided sufficient rotation curve and morphological resolution.

This work therefore links observable bar–ring morphology directly to both local dynamical conditions and the global cosmological timeline, providing a new tool for constraining galaxy formation scenarios. The agreement between independent modelling approaches indicates that the $\rho_c \propto t^{-2}$ scaling is not an artefact of any single assumption, but an intrinsic property of the galaxy–cosmos connection. Future work should extend this method to higher-redshift galaxies and marginalize over cosmological parameter sets to test the robustness of the onset timeline against uncertainties in $H(z)$.

REFERENCES

[1]de Haas, E. P. J. (2025) Spiral Arms as Fossil Tracers of Cosmic Expansion: Inferring Galaxy Formation Epochs from Pitch Angle Morphology. *viXra:2507.0021,* preprint https://https:

//vixra.org/abs/2507.0021.

[2]de Haas, E. P. J. (2018) A 'constant Lagrangian' RMW-RSS quantified fit of the galaxy rotation curves of the complete SPARC database of 175 LTG galaxies.. *viXra.org:Astrophysics,* p. https://vixra.org/abs/1908.0222.

[3]de Haas, E. P. J. (2025) One Single Metric Model's Unifying Perspective on Four Issues with Galactic Dynamics: B-TF Relation, Rotation Curves, Spirals and SMBH-Growth. *viXra:2506.0097,* preprint https://vixra.org/abs/2506.0097.

[4]McGaugh, S. S., Lelli, F., and Schombert, J. M. (2016) Radial Acceleration Relation in Rotationally Supported Galaxies. *Physical Review Letters,* **117**(20), 201101.

[5]Bromm, V. and Yoshida, N. (2011) The First Galaxies. *Annual Review of Astronomy and Astrophysics,* **49**, 373–407.

[6]Dayal, P. and Ferrara, A. (2018) Early galaxy formation and its large-scale effects. *Physics Reports,* **780**, 1–64.

[7]Buta, R. J. (2013) Galaxy Morphology. In *Planets, Stars and Stellar Systems* Vol. 6, pp. 1–63 Springer.

[8]Collaboration, P., Aghanim, N., Akrami, Y., et al. (2020) Planck 2018 results. VI. Cosmological parameters. *Astronomy & Astrophysics,* **641**, A6.

[9]Law, D. R., Shapley, A. E., Steidel, C. C., Reddy, N. A., Christensen, C. R., and Erb, D. K. (2012) The Kiloparsec-scale Kinematics of High-redshift Star-forming Galaxies. *Nature,* **487**, 338–340.

[10]Yuan, T.-T., Richard, J., Gupta, A., Kewley, L. J., Swinbank, M., Sobral, D., Livermore, R. C., and et al. (2017) A Dynamically Cold Disk Galaxy in the Early Universe. *Nature Astronomy,* **1**, 105.

[11]Tsukui, T. and Iguchi, S. (2021) Spiral morphology in an intensely star-forming disk galaxy more than 12 billion years ago. *Science,* **372**, 1201–1205.

[12]Gadotti, D. A. (2009) Structural properties of pseudo-bulges, classical bulges and elliptical galaxies: a Sloan Digital Sky Survey perspective. *MNRAS,* **393**(4), 1531–1552.

[13]Hopkins, P. F., Bundy, K., Croton, D., Hernquist, L., Keres, D., Khochfar, S., Stewart, K. R., Wetzel, A. R., and Younger, J. D. (2010) Mergers and Bulge Formation in ΛCDM: Which Mergers Matter?. *ApJ,* **715**(1), 202–229.

[14]Genel, S., Vogelsberger, M., Springel, V., and et al. (2014) Introducing the Illustris Project: the evolution of galaxy populations across cosmic time. *MNRAS,* **445**(1), 175–200.

[15]Pillepich, A., Nelson, D., Hernquist, L., and et al. (2019) First results from the IllustrisTNG simulations: the stellar mass content of groups and clusters of galaxies. *MNRAS,* **490**(3), 3196–3233.

[16]Fudamoto, Y. and et al. (2022) JWST detection of massive disk galaxies at $z > 3$. *Nature,* **604**, 260–264.

[17]Nelson, E. J. and et al. (2023) The emergence of massive galaxy disks in the early universe with JWST. *ApJL,* **943**(2), L9.

[18]Sofue, Y. and Rubin, V. (2001) Rotation Curves of Spiral Galaxies. *Annual Review of Astronomy and Astrophysics,* **39**(1), 137–174.

Appendix: Additional fits of galaxies from the SPARC database [4]

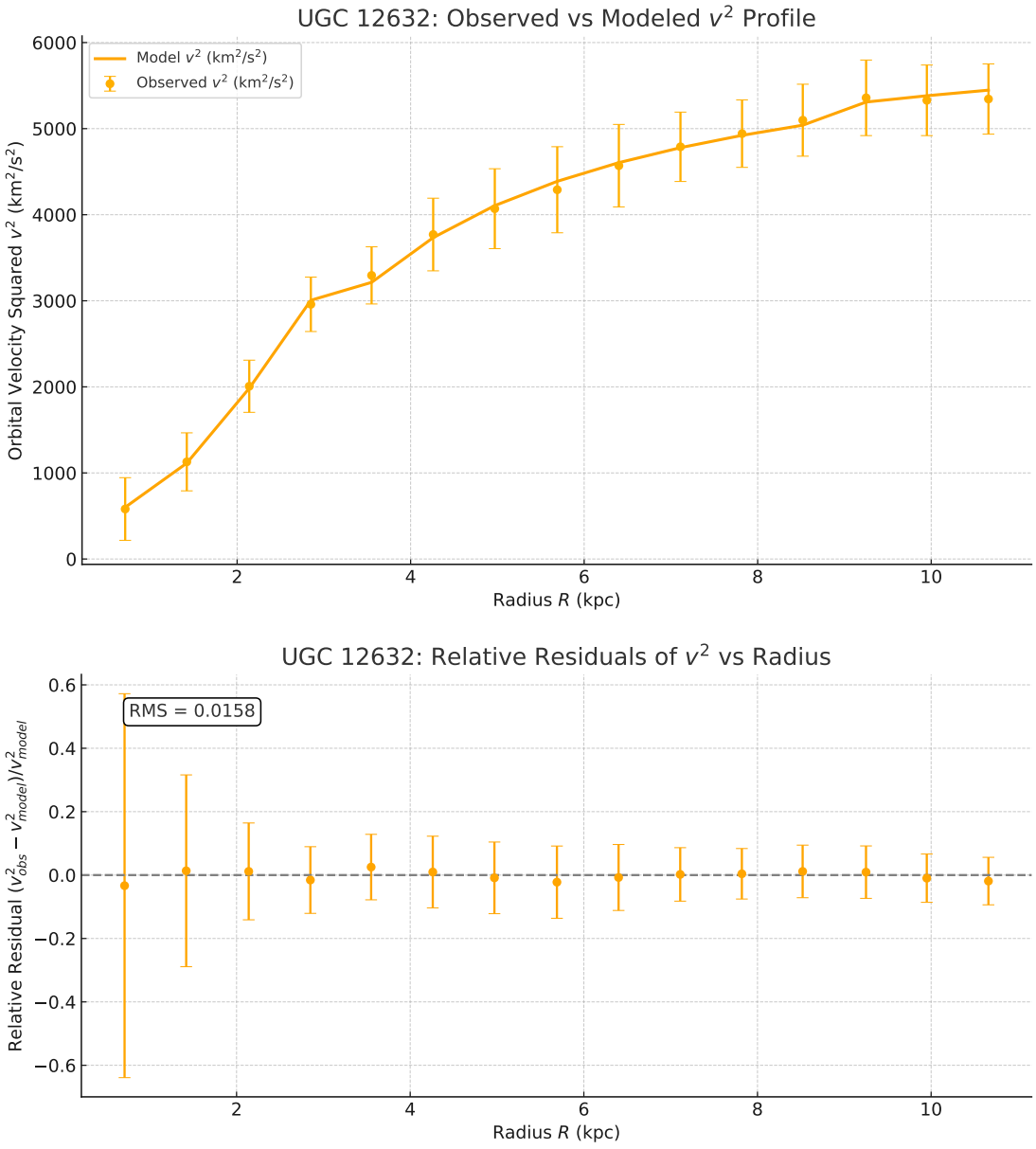

FIG. 17. **Top:** Observed squared orbital velocity v^2 (with error bars) versus radius R for galaxy UGC 12632, compared to the model prediction based on a constant Lagrangian approach. **Bottom:** Relative residuals $(v^2_{\text{obs}} - v^2_{\text{model}})/v^2_{\text{model}}$ with corresponding propagated uncertainties. The RMS of the relative residuals is 0.0158.

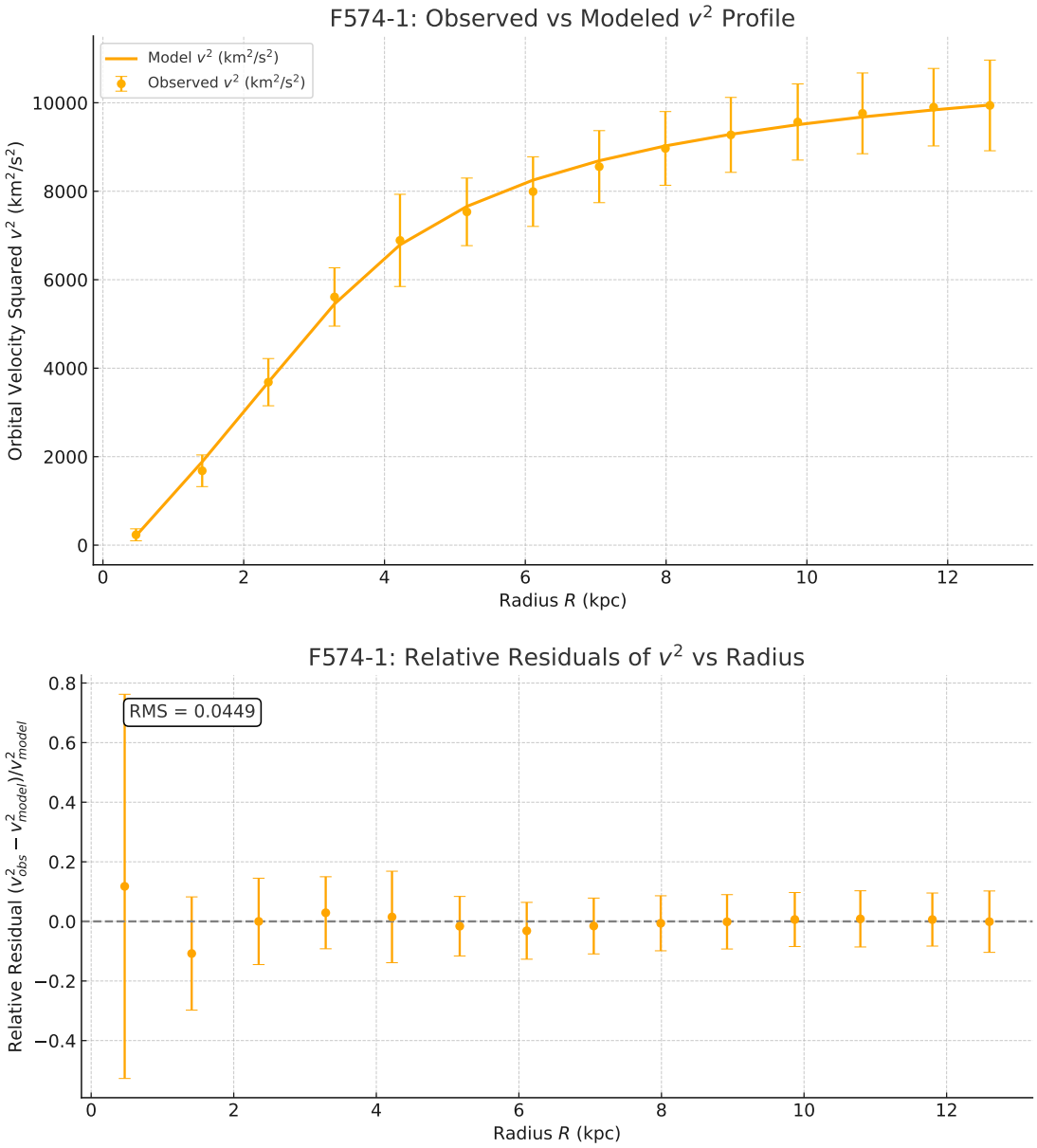

FIG. 18. **Top:** Observed squared orbital velocity v^2 (with error bars) versus radius R for galaxy F574-1, compared to the model prediction based on a constant Lagrangian approach. **Bottom:** Relative residuals $(v^2_{\text{obs}} - v^2_{\text{model}})/v^2_{\text{model}}$ with corresponding propagated uncertainties. The RMS of the relative residuals is 0.0449.

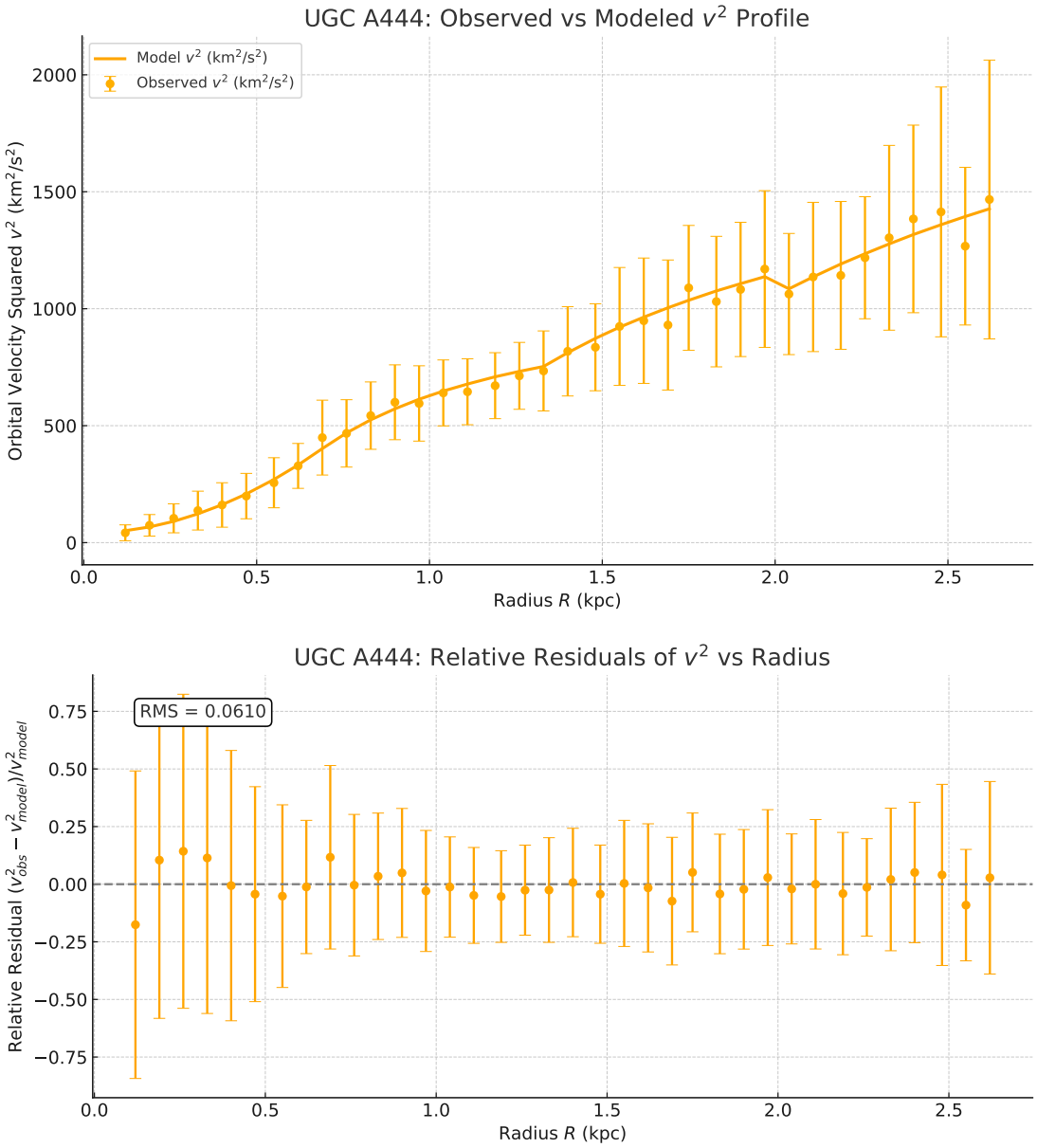

FIG. 19. **Top:** Observed squared orbital velocity v^2 (with error bars) versus radius R for galaxy UGC A444, compared to the model prediction based on a constant Lagrangian approach. **Bottom:** Relative residuals $(v^2_{\text{obs}} - v^2_{\text{model}})/v^2_{\text{model}}$ with corresponding propagated uncertainties. The RMS of the relative residuals is 0.0610.

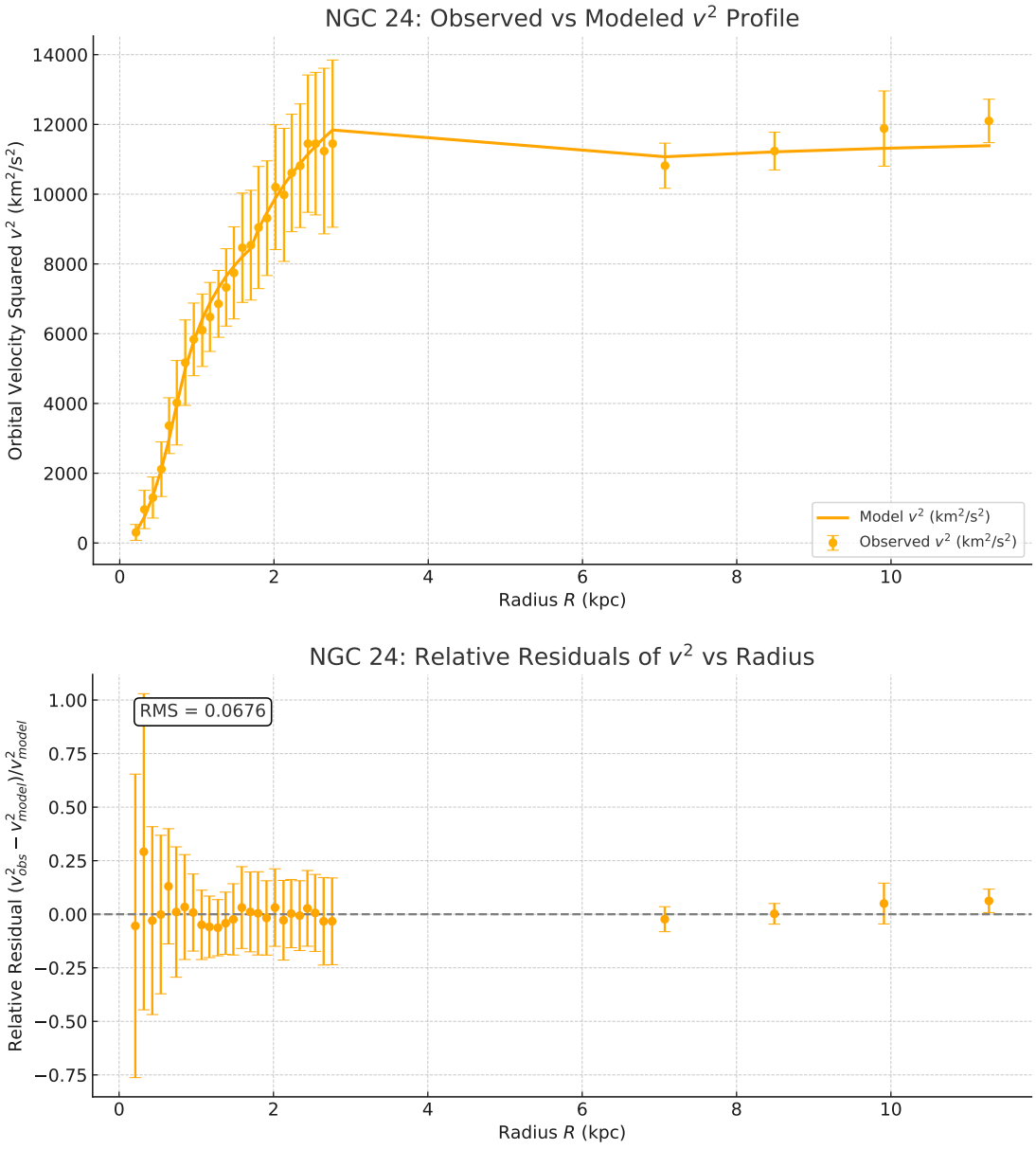

FIG. 20. **Top:** Observed squared orbital velocity v^2 (with error bars) versus radius R for galaxy NGC 24, compared to the model prediction based on a constant Lagrangian approach. **Bottom:** Relative residuals $(v^2_{\text{obs}} - v^2_{\text{model}})/v^2_{\text{model}}$ with corresponding propagated uncertainties. The RMS of the relative residuals is 0.0676.

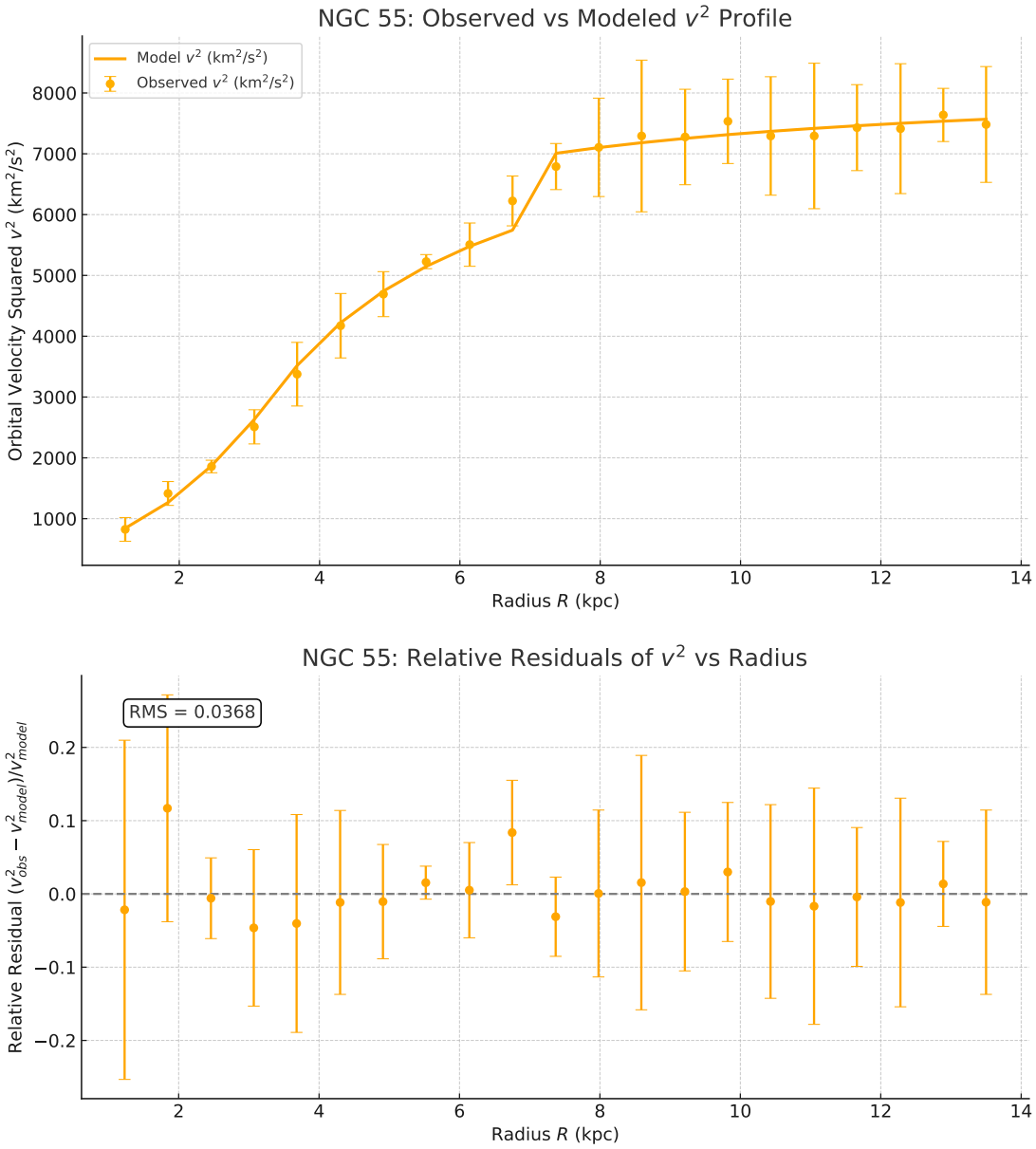

FIG. 21. **Top:** Observed squared orbital velocity v^2 (with error bars) versus radius R for galaxy NGC 55, compared to the model prediction based on a constant Lagrangian approach. **Bottom:** Relative residuals $(v^2_{\text{obs}} - v^2_{\text{model}})/v^2_{\text{model}}$ with corresponding propagated uncertainties. The RMS of the relative residuals is 0.0368.

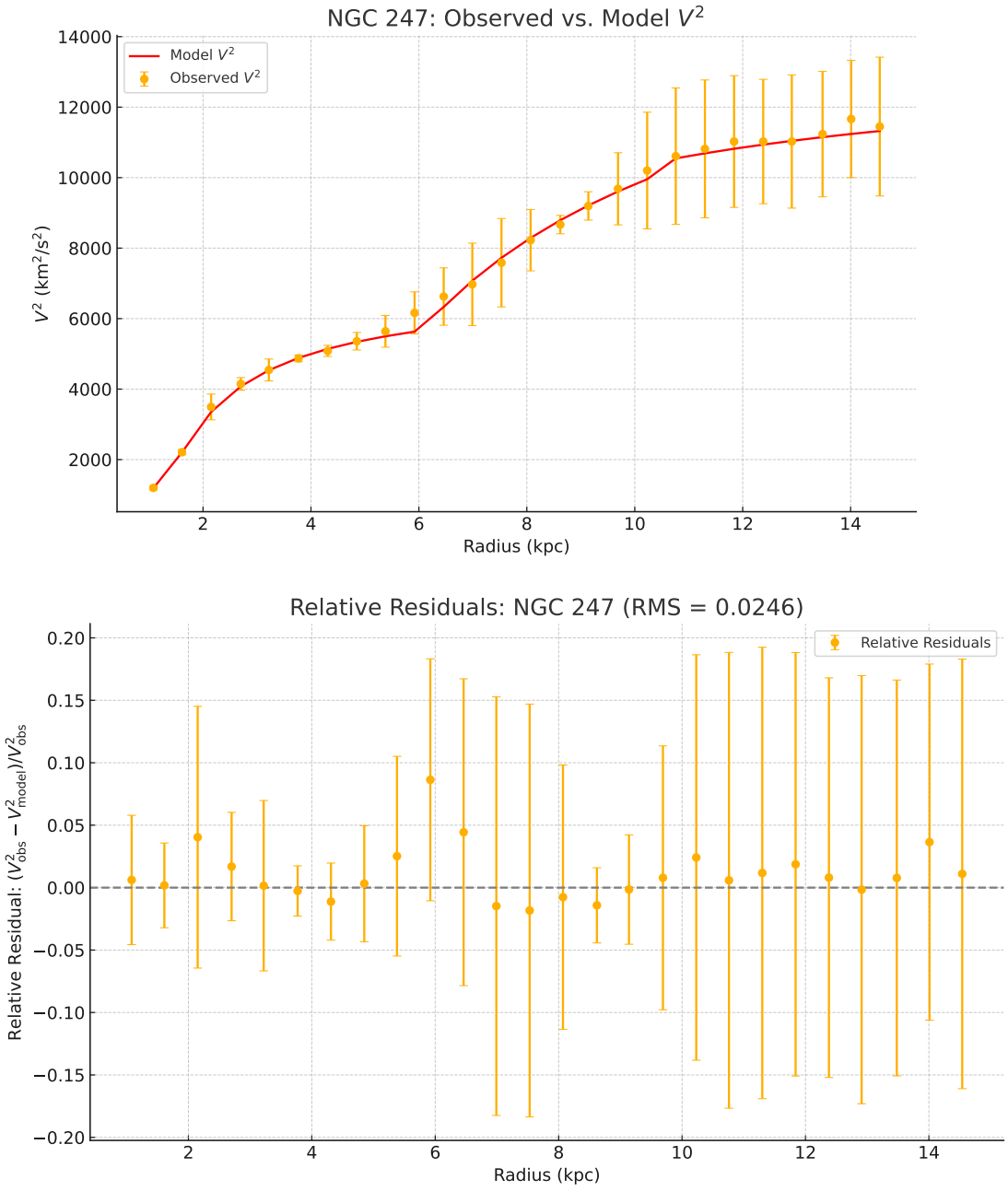

FIG. 22. **Top:** Observed squared orbital velocity v^2 (with error bars) versus radius R for galaxy NGC 247, compared to the model prediction based on a constant Lagrangian approach. **Bottom:** Relative residuals $(v^2_{\rm obs} - v^2_{\rm model})/v^2_{\rm model}$ with corresponding propagated uncertainties. The RMS of the relative residuals is 0.0246.

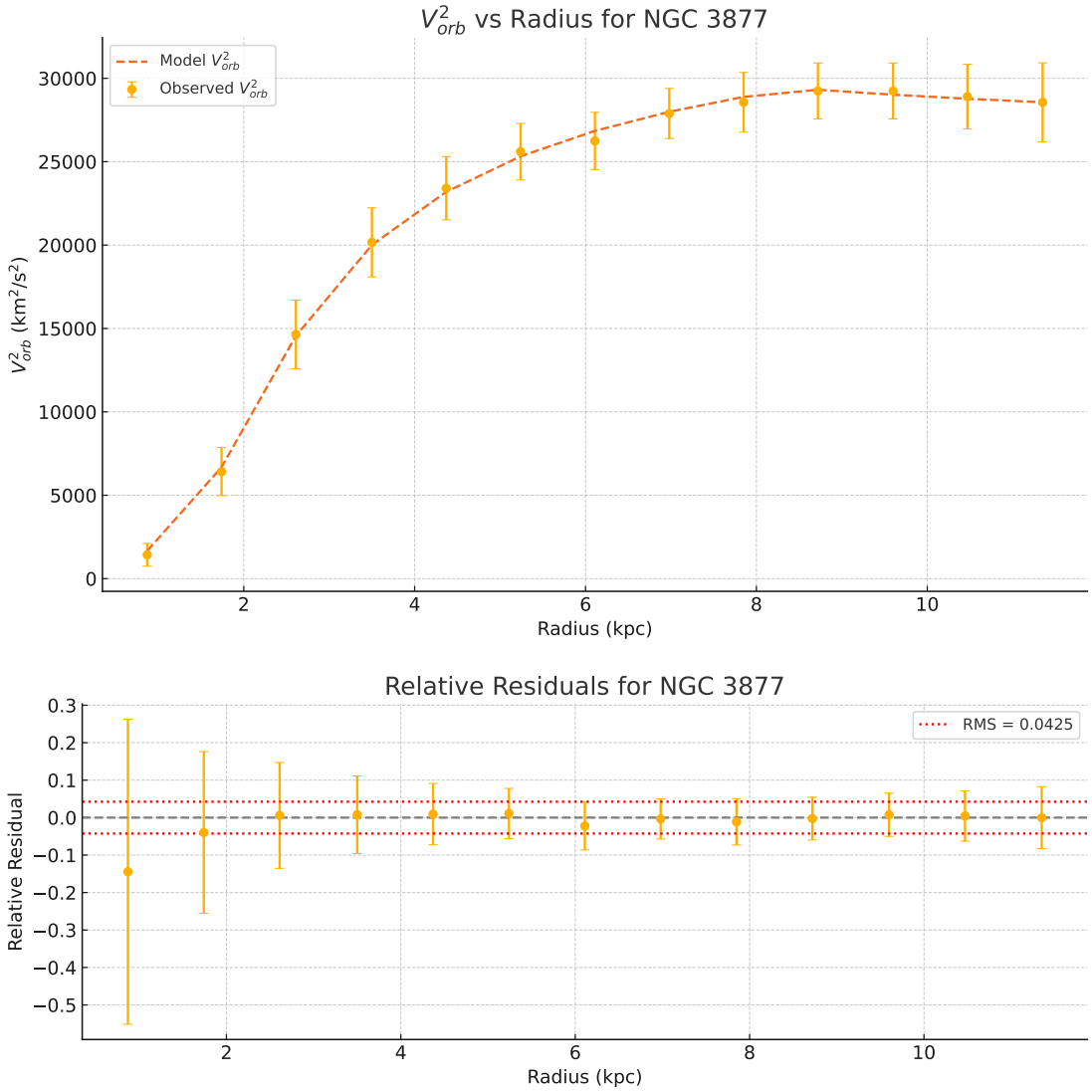

FIG. 23. **Top:** Observed squared orbital velocity v^2 (with error bars) versus radius R for galaxy NGC 3877, compared to the model prediction based on a constant Lagrangian approach. **Bottom:** Relative residuals $(v^2_{\text{obs}} - v^2_{\text{model}})/v^2_{\text{model}}$ with corresponding propagated uncertainties. The RMS of the relative residuals is 0.0425.

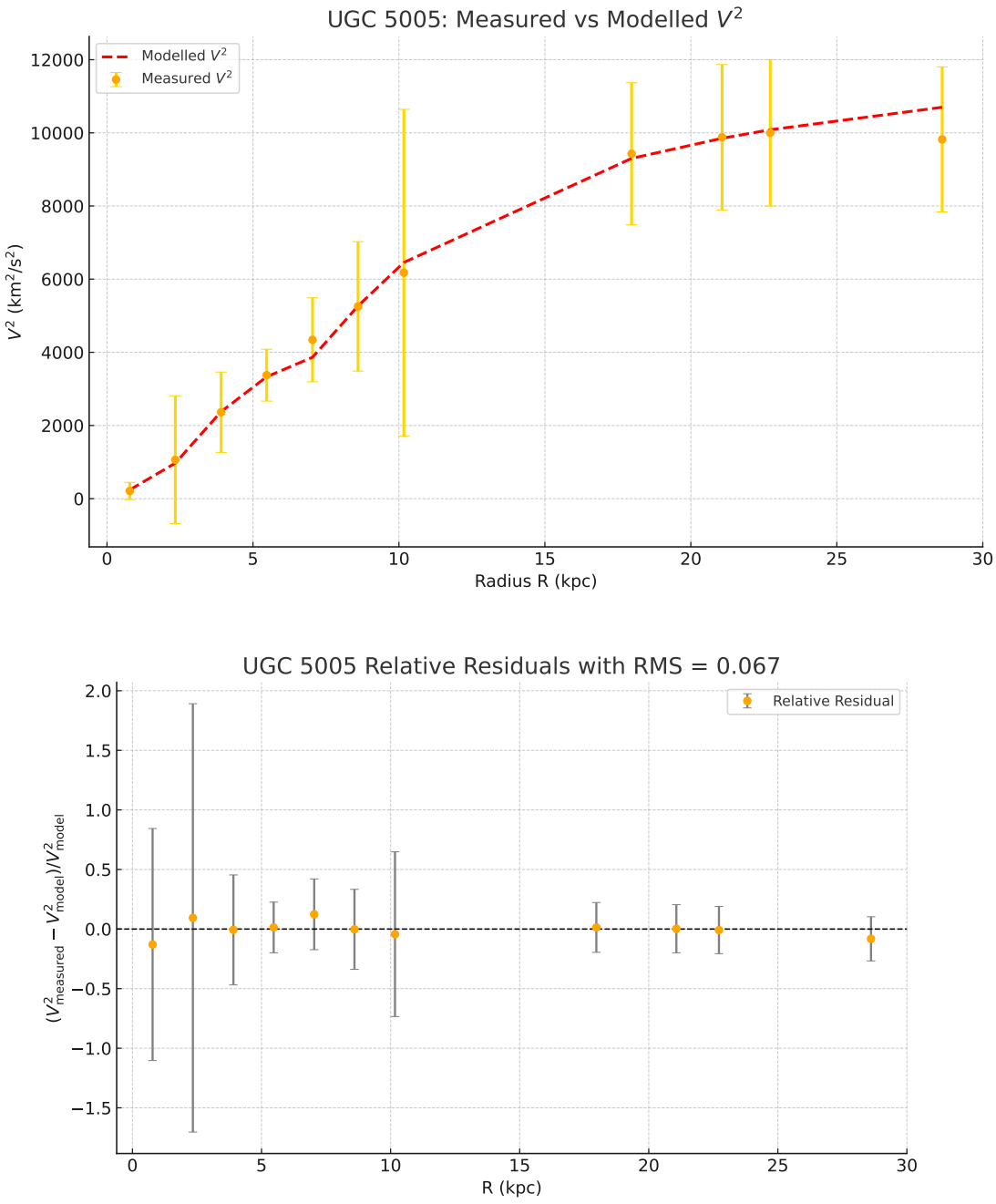

FIG. 24. **Top:** Observed squared orbital velocity v^2 (with error bars) versus radius R for galaxy UGC 5005, compared to the model prediction based on a constant Lagrangian approach. **Bottom:** Relative residuals $(v^2_{\text{obs}} - v^2_{\text{model}})/v^2_{\text{model}}$ with corresponding propagated uncertainties. The RMS of the relative residuals is 0.067.